STUDY OF THE PHASE BEHAVIOR OF HYDROCARBONS UNDER THE CONFINEMENT EFFECT USING MOLECULAR SIMULATION

A Dissertation

by

RAN BI

Submitted to the Office of Graduate and Professional Studies of
Texas A&M University
in partial fulfillment of the requirements for the degree of

DOCTOR OF PHILOSOPHY

Chair of Committee,	Hadi Nasrabadi
Committee Members,	Sara Abedi
	Eduardo Gildin
	Kan Wu
Head of Department,	Jeff Spath

August 2020

Major Subject: Petroleum Engineering

ABSTRACT

The phase behavior of hydrocarbons in shale reservoirs has garnered increasing attention in the petroleum industry. Significant differences in the phase behavior of petroleum fluids between conventional reservoirs and shale reservoirs have been observed. Because of the existence of nano-scale porous media in shale reservoirs, there are substantial surface–fluid interactions that can lead to a heterogeneous distribution of molecules and an alteration of the fluid phase behavior. In this work, we use Monte Carlo molecular simulation to investigate the confinement effect on the phase behavior of reservoir fluids in different models. Gauge Gibbs ensemble Monte Carlo (gauge-GEMC) and grand canonical Monte Carlo (GCMC) simulations are used to study the saturation pressure, adsorption, desorption, and hysteresis effect of single-component fluids in nanopores. Moreover, a simplified pore size distribution (PSD) model is proposed to investigate the effect of the PSD in shale rocks, and a multi-scale model in molecular simulation is created for the first time to mimic the nano-scale and macro-scale (macro-pores and fractures) porous media in shale rocks. We are also the first to use the Gibbs ensemble Monte Carlo (GEMC) simulation at imposed pressures to simulate the constant composition expansion (CCE) experiment for multi-component hydrocarbon mixtures in the multi-scale pore model. Our results show that 1) the critical temperature, critical pressure, and saturation pressure of single-component fluids decrease in nanopores; 2) the smaller the nanopore is, the stronger the confinement effect becomes and the further the phase diagram shifts; 3) when multiple pores exist in the fluid system, the fluids in larger pores take priority over those in smaller pores in vaporization, while the fluids in smaller pores have priority in condensing; 4) PSD can lead to an overall confinement effect in which it may be possible to use a single-pore model to represent the pore system of a shale sample; 5) in the multi-scale model, the confinement effect will cause a significant difference between the compositions of the fluids in different regions, where the fluid in the bulk region is leaner than that in the confined region and the difference in compositions will increase as the pressure decreases; and 6) the confinement effect in the multi-scale model may cause a significant shift or disappearance of the saturation pressure of the fluid in the bulk region.

ACKNOWLEDGMENTS

I would like to thank my committee chair Dr. Nasrabadi, my committee members, Dr. Abedi, Dr. Gildin, and Dr. Wu for their guidance and support throughout the course of this research.

Thanks to Texas A&M High Performance Research Computing (HPRC) Facility for their support.

Thanks also go to my colleagues in Dr. Nasrabadi’s research group for their assistance with this research.

Finally, I appreciate the encouragement, patience, and love of my family.

CONTRIBUTORS AND FUNDING SOURCES

Contributors

This work was supervised by a dissertation committee consisting of Professor Hadi Nasrabadi (Douglas Von Gonten Faculty Fellow) of the Department of Petroleum Engineering, Professor Sara Abedi (C.J. Craft Faculty Fellow) of the Department of Petroleum Engineering and Department of Civil Engineering, and Professors Eduardo Gildin (Ted H. Smith ’75 and Max R. Vordenbaum ’73 DVG Development Professor; Energi Simulation Chair in Robust Reduced Complexity Modeling) and Kan Wu (Chevron Corporation Faculty Fellow) of the Department of Petroleum Engineering.

All simulation work was supported by the Texas A&M High Performance Research Computing (HPRC) Facility.

The analysis depicted in Section 3.1.1 was conducted in part by Dr. Bikai Jin who was in Dr. Nasrabadi’s research group and was published in 2017.

Funding Sources

This research is sponsored by the Crisman Institute for Petroleum Research at Texas A&M University.

NOMENCLATURE

CBMC	Configurational–Bias Monte Carlo
CCE	Constant Composition Expansion
COM	Center of Mass
DSC	Differential Scanning Calorimetry
EOS	Equation of State
Gauge-GEMC	Gauge Gibbs Ensemble Monte Carlo
GCMC	Grand Canonical Monte Carlo
GEMC	Gibbs Ensemble Monte Carlo
GOR	Gas–Oil Ratio
HPRC	High Performance Research Computing
LJ	Lennard Jones
LRS	Liquid-Rich Shale
NIST	National Institute of Standards and Technology
NPT-GEMC	Pressure Imposed Gibbs Ensemble Monte Carlo
NVT-GEMC	Volume Imposed Gibbs Ensemble Monte Carlo
MCCCS	Monte Carlo for Complex Chemical Systems
PR EOS	Peng–Robinson Equation of State
PR-C EOS	Confined Peng–Robinson Equation of State
PSD	Pore Size Distribution
c_{1-4}	Constants in the torsion energy computation

d	Distance between a particle to the pore surface
F	Hypergeometric function
$\overrightarrow{F_k}$	Intermolecular force acting on a molecule *k*
k	Number of trial positions for a new atom
k_B	Boltzmann constant
k_θ	Constant in bond–bending potential energy
n	Number of moles
N	Number of molecules
N_a	Avogadro number
P	Pressure
P_{acc}	Acceptance probability
P_b	Bubble point pressure
P_0	Reference pressure
q	Random number between 0–1
r	Distance from the pore surface
r_{cutoff}	Cutoff distance of the potential energy computation
r_{ij}	Distance between particles *i* and *j*
$\overrightarrow{r_k}$	Random location of an atom *k*
R	Pore radius in the Steele 10-4-3 potential
R_{gas}	Gas constant
T	Time

$u(r)$	Increment of potential energy with the atom in position *r*
U	Potential energy
U_{bend}	Bond–bending potential energy
U_{ext}	External potential energy
U_{Steele}	Total interaction energy in the Steele 10-4-3 potential
U_{tors}	Torsion energy
V	Volume
α	Constant in the Steele 10-4-3 potential
ρ	Density
ρ_S	Volumetric density of multi-layer graphite
μ	Chemical potential
μ_0	Chemical potential under a reference pressure
σ_{ij}	Distance between particles *i* and *j* when the interaction is zero
ϵ_{ij}	Potential well depth for particles *i* and *j*
θ	Angle between two bonds
ϕ	Dihedral angle
Δ	Distance between graphite layers
Δr	Length of the intervals in the density profile generation
ΔU	Change of potential energy
ΔV	Change of volume
$\Delta\mu/k_B$	Change of chemical potentials in GCMC simulations
$\mathit{\Gamma}$	Gamma function

TABLE OF CONTENTS

Page

LIST OF FIGURES

LIST OF TABLES

Page

1. INTRODUCTION

1.1. Problem Statement

Shale resources have played an essential role in oil and gas production in the U.S. The production of tight oil and gas has become a significant supply of energy over the past few years. Shale reservoirs are complicated. Knowledge of hydrocarbon phase behavior is necessary for reserve estimations, reservoir simulations, production forecasting, and enhanced oil recovery [1–3]. However, understanding the phase behavior of hydrocarbons in shale reservoirs remains one of the challenges in their exploitation.

During the production of shale reservoirs, engineers have observed many anomalous production phenomena. Whitson and Sunjerga [4] demonstrate that the liquid yield produced from a liquid-rich shale (LRS) has always been observed to be much leaner than what would be produced from a conventional reservoir containing the same initial reservoir fluid system. An anomalously high producing gas–oil ratio (GOR) and substantial recovery loss compared to a conventional reservoir have been found [4,5]. For LRS gas condensate reservoirs, it will mainly produce the solution condensate being carried by the flowing reservoir gas, which means that the oil forming by condensation in the reservoir will remain unproduced. Numerous field studies [6–8] have reported that a relatively flat production GOR over a significantly long period (several years) has been observed in unconventional volatile-oil reservoirs, even when the bottom-hole pressure and the pressure around the wells have been below the bubble point pressure. The production GOR stays constant and close to the initial production GOR. PVT properties of reservoir fluids from traditional laboratory tests are not able to estimate behaviors such as those mentioned above.

Shale rocks contain pores from sub-10 nm to over 100 nm [9]. Unlike conventional reservoirs where most of the pores are macropores (diameters larger than 50 nm), a significant amount of pores in shale reservoirs are mesopores (diameters between 2 and 50 nm) and micropores (diameters less than 2 nm) [10]. The volume of mesopores and micropores can reach around 40% of the total pore volume [11]. In macropores, reservoir fluids are found in the bulk condition, where interactions between the pore surface and reservoir fluids (surface–fluid interactions) are negligible compared to the interactions between reservoir fluids (fluid–fluid interactions). The phase behavior of reservoir fluids in the bulk condition can be well described by several equations of state (EOS's); for example, Peng–Robinson EOS (PR EOS) [12,13] and Soave–Redlich–Kwong EOS [14], which have been proposed in past decades. These traditional EOS's do not take into account the surface–fluid interactions. However, in the mesopores and micropores, where the pore sizes are comparable to the sizes of reservoir fluid molecules, the surface–fluid interactions become significant and dominant. Numerous studies have shown that the surface–fluid interactions in mesopores and micropores can lead to a heterogeneous distribution of molecules and an alteration of the phase diagram [1,15–18], which is usually called the confinement effect. The smaller the pores are, the more significant the confinement effect becomes.

Challenges in the phase behavior study of reservoir fluids in shale reservoirs are not limited to the consideration of surface–fluid interactions. In reservoir rocks, pores of different sizes occupy various volume percentages, which is described as pore size distribution (PSD) [9,11,19–21]. The PSD in shale reservoirs varies between regions and samples [9]. Because the phase behavior of reservoir fluids in the mesopores and micropores is pore-size dependent and needs to be described differently from the bulk condition, the PSD effect needs to be considered in the phase behavior study. Thermodynamically, shale reservoirs are multi-scale systems that can be divided into two regions. The generated hydraulic fractures and macropores in the shale reservoirs form the macro-scale porous media (bulk region), and the mesopores and micropores in the shale reservoirs build the nano-scale porous media (confined region) [16]. The bulk region and the confined region are connected and hydrocarbon molecules can exchange between these two regions. The reservoir fluids can stay in the equilibria state inside these regions. This requires a multi-scale (macro-scale + nano-scale) model to properly understand the hydrocarbon phase behavior in shale systems.

1.2. Review of Current Techniques

Several experiments have been used to investigate the phase behavior of hydrocarbons in confined porous media. Controlled pore glass, MCM-41, and SBA-15 are materials widely used to build confined porous media in experimental conditions. Isothermal curves are generated in these experiments to study the adsorption, desorption, and hysteresis under the confinement effect [22–28]. The differential scanning calorimetry (DSC) method has been used to measure the bubble point temperature of single-component fluids and mixtures at atmospheric pressure by Luo et al. [29–32]. Lab-on-a-chip devices have been developed in recent years to estimate the dew point and bubble point of pure hydrocarbons by observation through inverse confocal microscopy [17,33–40]. Compared to other experimental techniques, this technique requires a small amount of the testing fluid and has advantages in visualization. Recent advances in micro- and nano-fabrication techniques have enabled people to fabricate nanochannels as small as 2 nm on the lab-on-a-chip platforms [41]. Previous experimental studies have demonstrated that there are no significant changes in the phase behavior of the fluid in nanopores with diameters larger than 30 nm [29–31,34–40]. Although measuring the confinement effect on the phase behavior of hydrocarbons by experiments is accurate, it is hard to implement tests using multi-component mixtures under reservoir conditions because of the restrictions of these devices.

Cubic EOS modeling is one of the most popular and efficient techniques to study the phase behavior of reservoir fluids in the bulk condition (conventional reservoirs). In terms of the phase behavior study of reservoir fluids under the confinement effect (reservoir fluids in shale nanoporous media), using traditional EOS's alone is not sufficient. One of the most considered approaches is to couple the capillary pressure that is calculated by the Young-Laplace equation with the traditional EOS's [6,26,42–46]. This method considers the pressure difference between the vapor and liquid phases in nanopores. Nojabaei et al. [6], Du and Chu [43], and Zhang et al. [45] studied the capillary effect on the phase behavior of Bakken oil and performed the history matching of the flowing bottom-hole pressure and flow rate. They claim that by considering the effect of the capillary pressure, the history matching becomes more accurate. Zhang et al. [45] also found an increase in the cumulative oil/gas production and recovery. Nojabaei et al. [46] used an in-house compositional reservoir simulator to study the effect of capillary pressure on phase behavior in tight rocks and shales. An increased original oil in place and a higher cumulative oil production were reported by considering the effect of capillary pressure. Traditional EOS's can also be modified by adjusting the critical properties (critical temperature and pressure) of each component [44,47,48]. The altered critical properties of each component in nanopores are required to be obtained in advance by other methods, such as molecular simulation and experiments. This method also assumes shale rocks contain nanopores of a single size, so PSD is not considered. Recently, Travalloni et al. [49] have extended the PR EOS to investigate the phase equilibrium of the fluids confined in porous media. The new EOS (PR-C EOS) describes the phase behavior of reservoir fluids as a function of pore diameter. When the pore diameter is large (bulk condition), the PR-C EOS is equivalent to the PR EOS, while under the confinement effect, the PR-C EOS considers the surface–fluid interactions using a square-well potential. To quantify the surface–fluid interactions, the PR-C EOS requires extra parameters (square-well potential depth and width) of each component, which can be measured by experiments. Luo et al. [31] applied the PR-C EOS to investigate phase transitions of hexane, octane, and decane in nanopores with diameters in the range of 2.2–37.9 nm. They obtained good agreement between the modeling and DSC experimental results. Luo et al. [3] later implemented the PR-C EOS to a multi-scale fluid phase behavior simulation and performed a compositional reservoir simulation using the confined PVT properties of the reservoir fluid. The phase behavior simulation results indicated that the bubble point pressure (P_b) became lower because of the confinement effect. They obtained reduced cumulative oil and gas production and increased production GOR compared to the conventional reservoir condition.

Monte Carlo simulation is a statistical method based on the description of the interactions between atoms or molecules. Because it can describe the heterogeneous distribution of particles without additional assumptions, the Monte Carlo simulation has become another widely used method to study phase behavior in shale reservoirs [18,50–52]. With increased computer capacity, the scope of the Monte Carlo simulation has been extended significantly. The Monte Carlo simulation has various statistical ensembles, including a canonical ensemble (NVT ensemble), isothermal-isobaric ensemble (NPT ensemble), grand canonical ensemble (μVT ensemble), and Gibbs ensemble (either NVT or NPT) [53]. The canonical ensemble and isothermal-isobaric ensemble can be used to compute the single-phase properties of a system (i.e., compressibility, density, chemical potential, and Joule-Thomson coefficient) [54–58]. The grand canonical Monte Carlo (GCMC) simulation defines a system with specified chemical potential (μ), volume (V), and temperature (T). It is a widely used technique to study adsorption isotherms and hysteresis of either pure-component or multi-component systems in mesopores and micropores [59–61]. By modeling cases with a wide range of chemical potentials, the chemical potentials at which phase transitions happen are obtained and subsequently used to compute the condensation and vaporization pressure in the adsorption and desorption processes, respectively. Jin et al. modified the GCMC method by adding a gauge box to improve the efficiency of the original GCMC method when dealing with multi-component systems [1,62]. Panagiotopoulos [63] developed the Gibbs ensemble Monte Carlo (GEMC) simulation to study phase equilibria. It has two conditions: the global volume imposed (NVT-GEMC) and the pressure imposed (NPT-GEMC). The difference between the GEMC and NVT or NPT ensembles mentioned above is that GEMC involves two simulation boxes, in which phases can be separated in each box. The method avoids modeling the surface between phases explicitly so that computing the phase equilibrium becomes more efficient [53]. The NVT-GEMC defines the system with a fixed number of molecules (N), total volume (V), and temperature (T). It can be used to study both pure-component fluids and mixtures [26,58,63,64]. The coexistence pressure is usually determined using the gas phase pressure. Later, Neimark and Vishnyakov developed a more efficient NVT-GEMC (the gauge-GEMC) and successfully applied it to pure and binary substances in confined systems [65–67]. The gauge-GEMC simulation contains two simulation boxes in which one works as a gauge meter and the other represents the fluid system. The gauge meter box can constrain the density fluctuation in the fluid system and let the fluid stay in any state, which could be unstable [62]. Instead of fixing the total volume, the imposed pressure GEMC (NPT-GEMC) has the coexistence pressure specified in advance. Thus, the volume of each phase changes until the specified pressure is reached. It is applicable for mixtures only (because both phases would converge to the same density in the case of a single-component fluid). Panagiotopoulos et al. and Potoff et al. have used this method to study binary and ternary mixtures [68,69]. Nikolaidis et al. recently used this method to investigate the vapor–liquid equilibrium of binary methane mixtures with long n-alkanes for a wide range of temperatures and pressures. The obtained data was then used for consistent fitting of binary interaction parameters for equations of state [70].

In current work, the gauge-GEMC is used to study the phase behaviors of single-component fluids. Phase diagrams of pure methane are generated based on single-pore models. Moreover, we perform the GCMC molecular simulations to model the adsorption isotherms of n-butane in a 2 nm slit channel. The hysteresis caused by the confinement effect of the 2 nm slit channel is quantified. Furthermore, we create a model to investigate the effect of the PSD on the confined phase behavior of methane. Last but not least, we modify the traditional NPT-GEMC to investigate the confinement effect on the phase behavior of reservoir fluids in shale multi-scale systems. For the first time, the constant composition expansion (CCE) experiments of multi-component mixtures in a shale multi-scale system are modeled using molecular simulation. Steele 10-4-3 has been widely used to investigate the fluid wall interaction for planar graphite models [71–74]. In the present work, we use an extension of the Steele 10-4-3 potential to quantify the confinement effect acting on the fluids by the carbon nanotube cylindrical pore boundaries [75]. The saturation pressure is determined for each multi-scale system. Compositions, saturation pressures, liquid yield, and relative volume are discussed and compared with the computations without the confinement effect.

2. METHODOLOGY[*]

2.1. Monte Carlo Simulation

Monte Carlo simulation is a statistical thermodynamics technique that derives properties of a system by taking into account the individual position and conformation of every molecule. To reach the equilibrium state of a system, millions of Monte Carlo steps are executed during the simulation to achieve the global minimum of the free energy. At each Monte Carlo step, one of Monte Carlo moves is attempted.

The most commonly used Monte Carlo moves are the translation move (center of mass), rotation move, and partial regrowth move. For the center of mass translation move, a molecule in the system is chosen randomly. The entire chosen molecule is then displaced a random distance in a random vector direction. The rotation move is to rotate a randomly chosen molecule by a random angle. In this move, the internal bond distances, bending angles, and torsion angles of the selected molecule are kept the same. In terms of the partial regrowth move, a random atom is chosen in a random molecule. Then, one end of the chosen atom is cut off and allowed to regrow at a randomly selected position. The new configuration (state) after a Monte Carlo move is accepted with a probability. The acceptance criterion for a move is:

$$P_{acc} = min\left(1, exp\left(-\frac{1}{k_B T}(U_{new} - U_{old})\right)\right), \quad (1)$$

---

[*] Part of this chapter is reprinted with permission from "Molecular Simulation of the Constant Composition Expansion Experiment in Shale Multi-Scale Systems" by Ran Bi and Hadi Nasrabadi, 2019. *Fluid Phase Equilibria*, 495, 59-68, Copyright [2019] by Elsevier B.V.

where P_{acc} is the acceptance probability, k_B is the Boltzmann constant which equals 1.381×10^{-23} J/K, T is the temperature, and U_{new} and U_{old} are the potential energy of the new and the old configurations, respectively. The definition of the P_{acc} indicates that if $U_{new} < U_{old}$, in other words, $exp\left(-\frac{1}{k_B T}(U_{new} - U_{old})\right) > 1$, the Monte Carlo move and the new configuration are accepted. If $U_{new} > U_{old}$ or $exp\left(-\frac{1}{k_B T}(U_{new} - U_{old})\right) < 1$, a random number q between 0 and 1 is generated. The Monte Carlo move and the new configuration are accepted only when $exp\left(-\frac{1}{k_B T}(U_{new} - U_{old})\right) > q$. If any of the above moves are rejected, the old configuration is recounted in the Markov chain of states.

Some Monte Carlo moves are applied to specific ensembles. For the ensembles that contain more than one simulation boxes (the GEMC and the gauge-GEMC), a swap move is implemented. The swap move is used to move a randomly chosen molecule in an arbitrary simulation box to the other simulation box. This move makes it possible for the different phases in the system to have an equal chemical potential for every molecule type (species of components). For the ensembles with pressure imposed (the NPT ensemble and the NPT-GEMC), the volume of the system is allowed to fluctuate. Therefore, a volume change move is necessary. The volume change move is used to expand or shrink a randomly selected simulation box by a random amount of ΔV. In this move, the internal conformation of molecules and the dimensionless position of molecular centers of mass remain unchanged. Accordingly, every molecule is translated, but the translation vector varies from one to the other [53]. This move makes it possible for the system to achieve mechanical equilibrium. In terms of the GCMC ensemble, insertion and deletion moves are implemented. The insertion moves insert one type of molecule at a randomly selected position in the simulation box, while the deletion moves randomly delete one molecule of the selected type. It should be noted that, in a GCMC simulation, the attempts of insertion moves and the attempts of deletion moves should be equal. The acceptance probabilities of the specific moves are summarized in Table 1, where P_{acc}, k_B, T, U_{new}, and U_{old} are consistent with the definitions in Eq. (1). V is the volume, ΔU and ΔV represent the change of the potential energy and volume, respectively, and N_i and N represents the number of type i molecule and total molecules, respectively. The acceptance probability of the swap move indicates that a type i molecule is moved from simulation box A to box B. U_{ext} in the acceptance probabilities of the insertion and deletion moves is the external potential energy (intermolecular energy from the interaction between molecules), and $\bar{\mu}_i = \mu_i - \mu_{i0}$, where μ_{i0} is the chemical potential of a perfect gas of component i under a reference pressure P_0 and temperature T [53].

Table 1: Acceptance probabilities of the specific Monte Carlo moves.

Monte Carlo Moves	**Acceptance Probability**
Swap	$P_{acc} = min\left(1, \frac{N_i^A}{V^A} \frac{V^B}{N_i^B + 1} exp(-\frac{\Delta U^A - \Delta U^B}{k_B T})\right)$
Volume Change	$P_{acc} = min\left(1, \left(\frac{V + \Delta V}{V}\right)^N exp(-\frac{U_{new} - U_{old} + P\Delta V}{k_B T})\right)$
Insertion	$P_{acc} = min\left(1, \frac{V P_0}{(N_i + 1) k_B T} exp(-\frac{\Delta U_{ext} - \bar{\mu}_i}{k_B T})\right)$
Deletion	$P_{acc} = min\left(1, \frac{N_i k_B T}{V P_0} exp(-\frac{\Delta U_{ext} - \bar{\mu}_i}{k_B T})\right)$

The acceptance probability of a Monte Carlo move can be very low when inserting large molecules or a type of molecule into a condensed phase because the test position that is chosen randomly to insert the molecule can easily cause overlaps with other existing molecules around it. To improve the acceptance the insertions are working with another statistical Monte Carlo move called the configurational–bias Monte Carlo (CBMC) move. In the CBMC insertion move, the inserted molecule grows step by step. The insertion of the first atom in a molecule is arbitrary. However, several possible random locations (r_k, where $k = 1, \dots, k_{max}$) of the next atom are tested, and the final position of the next atom is determined by a probability [76]. The probability of the next atom to be placed in the position r_i is defined as

$$P(r_i) = exp\left(-\frac{u(r_i)}{k_B T}\right) / \sum_{k=1}^{k_{max}} exp\left(-\frac{u(r_k)}{k_B T}\right), \qquad (2)$$

where $u(r_i)$ is the increment of potential energy associated with the atom in position r_i [53]. In the present study, the CBMC move is used with the partial regrowth move, swap move, insertion move, and deletion move. We set 10 trial positions ($k_{max} = 10$) for each growing atoms when the CBMC is used.

Arithmetic averaging in the ensemble can easily obtain the values of volume, pressure, and energy. However, the chemical potential (μ) has to be evaluated using Widom tests [77–79]. The particle interaction energies obtained from attempted swap and insertion moves are used here to compute the chemical potential so that the chemical potential computation is performed with a minimal computational cost [68]. The calculated chemical potential can be used to check whether the equilibrium has been reached or not.

2.1.1. Gauge-GEMC Simulation

Gauge-GEMC is developed by Neimark and Vishnyakov [65–67] based on the NVT-GEMC technique developed by Panagiotopoulos [63] previously. It is a prevalent technique for computing fluid properties at equilibrium [1,66,80]. Two boxes are involved in the simulation: one represents the fluid system and the other one is used as a gauge meter (Fig. 1). The gauge-GEMC maintains the advantages of the original NVT-GEMC technique (the gauge-GEMC can investigate the phase equilibria of the fluid without modeling the surface between phases explicitly) and can control the fluctuations of the density and allow the fluid to stay in any state which could be unstable [53,62].

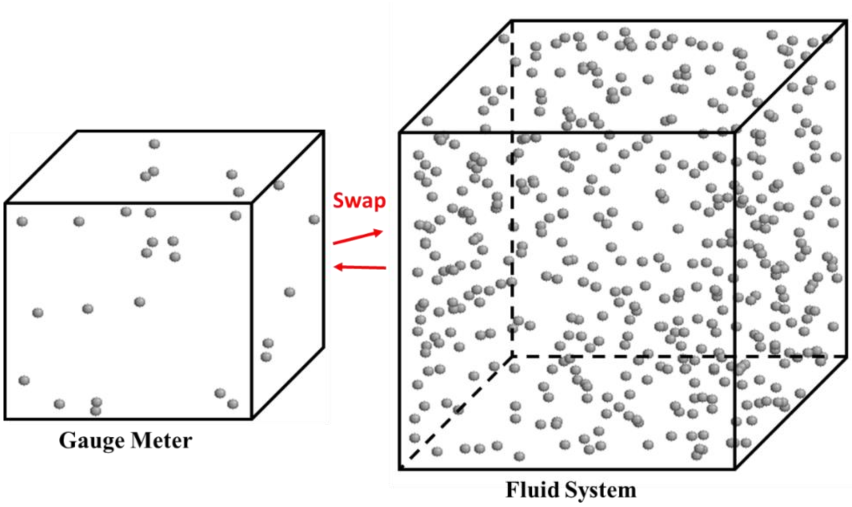

Figure 1: Schematic of the gauge-GEMC ensemble. Red arrows represent the swap move (particles are transferable between boxes). Grey balls are molecules which are methane in this example.

We use the gauge-GEMC simulation to study the phase behavior of single-component fluids in confined systems. The confined boundary (nanopores) will only be applied to the fluid system box, while the gauge meter box is in the bulk condition. The gauge-GEMC simulation includes a series of cases that are with the same volume and temperature but cover a range of numbers of molecules (see Fig. 8 in Section 3.1.1). For each case, simulations are performed in the constant number of molecules (N), total volume (V), and temperature (T) conditions. The volume of each box is fixed so that the total volume remains constant. In this study, random center-of-mass translation and rotation moves are implemented along with the swap move. These moves are designed to happen with the same probability at each Monte Carlo step.

This method can generate the complete phase diagram [e.g., chemical potential–density (μ–ρ) diagram] in the form of a van der Waals loop, including meta-stable and stable states. Phase equilibrium points can be computed from the μ-ρ relationship following the thermodynamic integration of Maxwell equal area rule [81] (see Fig. 8 in Section 3.1.1). A temperature–density (T–ρ) diagram can be generated by repeating the series of cases at various temperatures and collecting the vapor and liquid densities at equilibrium (see Fig. 9 in Section 3.1.1). Once a majority of equilibrium points at temperatures lower than the critical temperature are obtained, the critical point (critical temperature and density) can be extrapolated from simulation results at lower temperatures based on the rectilinear diameter law [82,83] and the density scaling law [84]. The density mentioned above is the average density inside pore spaces. The pressure at the phase equilibrium is computed by using the GCMC simulation as discussed in the next section.

2.1.2. GCMC Simulation

GCMC simulation is an efficient technique for studying adsorption isotherms and hysteresis in mesopores and micropores. Simulations are performed in a single simulation box at constant chemical potential (μ), volume (V), and temperature (T) conditions. During the GCMC simulation, the number of molecules is fluctuating to reach the imposed chemical potential at the specified volume and temperature. The increase and decrease of the number of molecules are achieved by insertion and deletion moves, respectively (Fig. 2). The configurational bias Monte Carlo (CBMC) method [53] is used for the generation of new molecules. To model the adsorption isotherms and hysteresis of the fluid in mesopores and micropores, a pore boundary (pore diameter is in several nanometers) will be added to the fluid system to model the confinement effect (see Fig. 5 in Section 2.3.2). Like the gauge-GEMC simulation, random center-of-mass translation and rotation moves are also implemented, and all the moves would happen with the same probability.

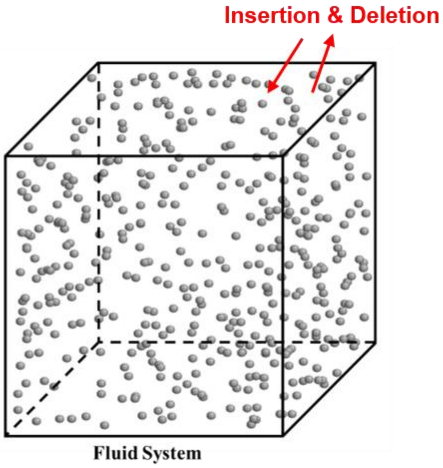

Figure 2: Schematic of the GCMC ensemble. Red arrows represent the insertion and deletion moves. Grey balls are molecules which are methane in this example.

A μ-ρ relationship can be obtained from a series of simulations with a range of chemical potentials (see Fig. 12 in Section 3.1.2). Phase transition (condensation or vaporization) is detected when a sharp density jump happens (condensation happens when the density of the fluid drops from a high value to a low value, while vaporization happens when the density of the fluid jumps from a low value to a high value). The chemical potential at which the phase transition happens is also determined accordingly. It should be noted that chemical potentials, in molecular simulations, are usually expressed in the form of diving by the Boltzmann constant (μ_i/k_B, where μ_i is the chemical potential of component i, and $k_B$is the Boltzmann constant).

Along with the isotherms and hysteresis study, in this work, the GCMC simulation has also been used to determine the pressure when confined systems exist. In the pressure computation, a GCMC simulation is performed in the bulk condition with the chemical potential obtained from simulations that contain the confined systems. The pressure calculated in the bulk condition is the external pressure of the confined systems [17,52]. For the vapor–liquid phase equilibrium study (the gauge-GEMC simulation in Section 2.1.1), once the chemical potential at the phase equilibrium has been determined, a GCMC simulation in the bulk condition with the calculated chemical potential and specified temperature will be performed to compute the pressure at the phase equilibrium. In terms of the study of adsorption isotherms, the phase transition pressure (condensation or vaporization pressure) can be computed in the same way as the phase equilibrium pressure except the chemical potential is substituted by the one when the phase transition happens.

The pressure computed directly from the confined systems cannot be compared to the normal pressure physically measured in experiments. The pressure calculated in the molecular simulation is called Virial pressure, which is obtained by the Virial equation [53]:

$$P = \frac{NR_{gas}T}{N_aV} + \frac{1}{3V}\langle \textstyle\sum_k \overrightarrow{r_k} \cdot \overrightarrow{F_k} \rangle, \tag{3}$$

where R_{gas} is the gas constant, $N_a = 6.022 \times 10^{23}$ mol^{-1} is the Avogadro number, $\overrightarrow{r_k}$ and $\overrightarrow{F_k}$ represent the position of the center of mass of molecule k and the intermolecular forces acting on the molecule k. The second term on the right side of the equation is called Virial term which is an ensemble average in Monte Carlo simulations (arithmetic average over a number of configurations). When the density of the system is very low or the molecular distribution in the system is homogeneous (e.g., in the bulk condition), the Virial term tends to be zero and the pressure expression reduces to the ideal gas law ($PV = NRT/N_a$). Due to the confinement effect of the pore boundary, the distribution of molecules in nanopores is highly heterogeneous. Therefore, the ideal gas assumption is not valid in nanopores. The principal values of the intermolecular force acting on a molecule vary significantly (the Virial term strongly depends on the local density). Therefore, the pressure calculated in the confined region can be very high and has different implications from that in the bulk condition [85].

2.1.3. NPT-GEMC Simulation

For the phase behavior investigation of multi-component mixtures at a certain pressure and temperature, we use the NPT-GEMC simulation. By using a separate simulation box for each phase, the explicit interfaces between fluid phases are not accounted for. During the simulation of the NPT-GEMC, a total number of molecules (N), pressure (P), and temperature (T) are fixed in advance, while phase volumes (V) are fluctuating independently.

The traditional NPT-GEMC simulation has two boxes that are in the bulk condition. To imitate the multi-scale systems in shale reservoirs, we modify the traditional model of the NPT-GEMC by adding an extra simulation box (Box III) with a fixed volume (the volume of Box III is constant). This extra box is designed to contain nanopores and act as the confined region (mesopores and micropores) in the fluid system. The other two boxes (Box I and Box II) remain the same as in the traditional NPT-GEMC boxes and thus act as the bulk region (macropores and fractures) in the system. A schematic of the system is shown in Fig. 3.

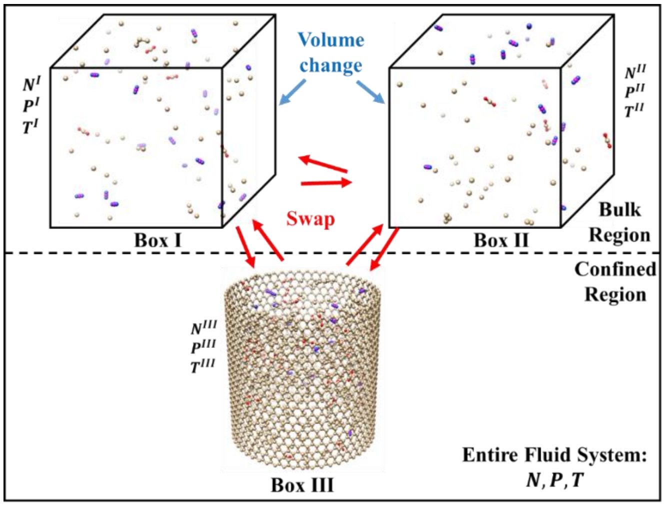

Figure 3: Schematic of the shale multi-scale system. The blue and red arrows indicate which boxes the volume change and swap moves are applied to, respectively. The entire fluid system is defined with constant N, P, and T. Adapted from [80].

In this multi-scale system, the total number of molecules N equals the summation of N^I, N^{II}, and N^{III}. The temperature of the system T is identical to the temperature of each box. The translation, rotation, and swap moves are applied to the molecules in all three boxes. The volume change move, however, is only applied to the boxes in the bulk region. The swap move makes each species in the different boxes have the same chemical potential. Corresponding to the imposed pressure, the volumes of Box I and Box II fluctuate to satisfy the mechanical equilibrium between the two phases. The pressure (P^{III}) of Box III is not expected to be equal to the imposed pressure P because the heterogeneous distribution of molecules in the nanopores makes the pressure computation (the Virial pressure) has different implications from that in the bulk region [85]. Systems at the internal equilibrium will obey the following conditions:

$$P = P^I = P^{II}, \tag{4}$$

$$\mu_i^I = \mu_i^{II} = \mu_i^{III}. \tag{5}$$

2.2. Potential Energy

The Lennard Jones (LJ) 12-6 potential is used to determine the intermolecular energy (non-bonded interactions), as follows:

$$U(r_{ij}) = 4\epsilon_{ij}\left[\left(\frac{\sigma_{ij}}{r_{ij}}\right)^{12} - \left(\frac{\sigma_{ij}}{r_{ij}}\right)^{6}\right], \tag{6}$$

where $U(r_{ij})$ is the LJ intermolecular energy, r_{ij} is the distance between particles i and j, σ_{ij} is the separation distance of particles i and j when the LJ interaction is zero, and ϵ_{ij} is the potential well depth of the minimum interaction energy. We apply the Lorentz-

Berthelot combining rule to determine the cross potential between unlike particles, as follows:

$$\sigma_{ij} = \frac{\sigma_{ii}+\sigma_{jj}}{2}, \tag{7}$$

$$\epsilon_{ij} = \sqrt{\epsilon_i \epsilon_j}. \tag{8}$$

In the current work, we apply the TraPPE-UA force field model [86] to all hydrocarbons, while the TraPPE-EH force field model [69] is applied to N_2 and CO_2, and the CHARMM [17] force field is applied to Si and O in amorphous silica boundaries. The LJ parameters of these models are listed in Table 2. In the TraPPE-EH force field, N_2 is treated as a three-site model, where both of the nitrogen atoms bonded to the center-of-mass (COM in Table 2) [69]. For bond-bending potential energy with the angle θ between two bonds, U_{bend} [87] is given by

$$U_{bend}(\theta) = \frac{k_\theta}{2}(\theta - 114)^2, \tag{9}$$

where k_θ is a constant ($k_\theta/k_B = 62500$ K/rad^2, in which k_B is the Boltzmann constant). Torsion energy is computed by the OPLS united-atom torsional potential [86], as follows:

$$U_{tors} = c_1[1 + cos\phi] + c_2[1 - cos(2\phi)] + c_3[1 + cos(3\phi)] \tag{10}$$

where ϕ is the dihedral angle, $c_1/k_B = 355.03$ K, $c_2/k_B = -68.19$ K, and c_3/k_B 791.32 K.

Table 2: Potential parameters in the Lennard Jones 12-6 potential.

	ϵ_{ii}/k_B (K)	σ_{ii} (Å)	**Source**
C (in graphite boundary)	30	3.7	TraPPE-UA [86]
CH_4	148	3.73	TraPPE-UA [86]
CH_3 (in n-alkane)	98	3.75	TraPPE-UA [86]
CH_2 (in n-alkane)	46	3.95	TraPPE-UA [86]
C (in CO_2)	27	2.8	TraPPE-EH [69]
O (in CO_2)	79	3.05	TraPPE-EH [69]
N (in N_2)	36	3.31	TraPPE-EH [69]
COM (in N_2)	0	0	TraPPE-EH [69]
O (in silica boundary)	61.39	3.09	CHARMM [17]
Si (in silica boundary)	46.80	3.70	CHARMM [17]

The distance beyond which the LJ potential is no longer computed is called truncated distance (r_{cutoff}). When the distance between two particles is not larger than the truncated distance ($r_{ij} \leq r_{cutoff}$), the interaction energy between them is computed by Eq. (6), while the interaction energy is negligible ($U_{ij} = 0$) if $r_{ij} > r_{cutoff}$. In the current work, the LJ potential is truncated at $r_{cutoff} = 10$ Å to avoid unnecessary computation, and a long-range tail correction is included. The same setting has also been applied in other studies, where molecular simulation results show a high consistency with the experimental results [53,69]. The electrostatic energy is only considered when CO_2 is contained in the mixtures. It is determined by using the Ewald summation [84]. The polarization energy is not considered in this paper. The Monte Carlo for Complex

Chemical Systems (MCCCS) Towhee [88] is modified to perform all the simulations in this work.

2.3. Pore Models

Periodic boundary conditions are applied to the simulation boxes to avoid a boundary effect. Simulation boxes which are in the bulk condition (e.g., the gauge meter box in the gauge-GEMC simulation, and Boxes I and II in the NPT-GEMC simulation) are repeating identical replicas in all space directions, while simulation boxes which contain confined fluid systems (e.g., the fluid system box in the gauge-GEMC and GCMC simulations, and the Box III in the NPT-GEMC simulation) are only replicating in the directions that have no pore boundaries. To use the minimum image convention method to compute molecular interactions with periodic boundary conditions, we ensure the sizes of boxes at all states are at least $2 \times r_{cutoff}$ [53,84].

2.3.1. Multi-Layer Graphite Cylindrical Pore Model

Since a majority of mesopores and micropores are formed in kerogen and one of the most significant elements in kerogen is carbon [89–91], graphite has been widely used in molecular simulations for modeling nano-scale pore boundaries [1,62,80]. In this work, for investigating the phase behavior of methane in cylindrical pores (the gauge-GEMC simulations), we model the pore boundaries explicitly using the multi-layer graphite.

A schematic of the multi-layer graphite cylindrical pore model is shown in Fig. 4. Graphite has a honeycomb structure with a bond length of 0.142 nm (Fig. 4a). The multi-layer graphite model is generated from a multi-layer graphite cube in which layer separation is 0.335 nm in the *z*-direction (Fig. 4b). To create the cylindrical features, we cut out redundant atoms and left a cylindrical pipe with a specific inner diameter and boundary thickness. The inner diameter of the pipe is the diameter of the cylindrical pore. In this work, we specify the thickness of the multi-layer graphite cylindrical pore is 4 Å (Fig. 4c). This pore model has been applied in the fluid system box in the gauge-GEMC simulation with a 1D periodic boundary condition in the *z*-direction (the gauge meter box in the gauge-GEMC simulation is kept in the bulk situation with 3D periodic boundary condition).

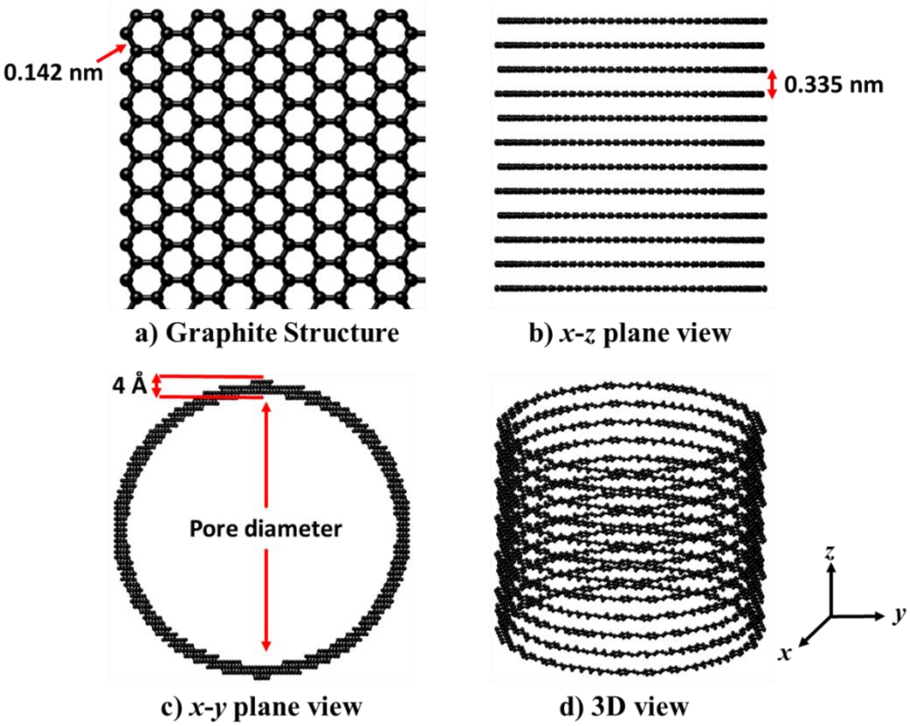

Figure 4: Schematic of the multi-layer graphite cylindrical pore model. a). graphite structure. b). *x-z* plane view of the model. c). *x-y* plane view of the model. d) 3D view of the model.

2.3.2. Amorphous Silica Slit Pore Model

The amorphous silica slit pore model has been used to study the adsorption isotherms and hysteresis of n-butane in a 2 nm confined system. We tend to use the amorphous silica slit pore to model some phase behavior experiments that have been done using lab-on-a-chip nanofluidic devices which are made of glass.

Based on the dimension of the channel in the nanofluidic devices, a slit-type pore is built following the strategy in Yang et al. [17]. We generate the pore boundary materials (amorphous silica) by annealing a cristobalite cube from 8000 K to 300 K. A 4 Å thickness layer of the amorphous silica is cut off from the cube and used as the top and bottom boundaries of the slit pore model (Fig. 5). This model has been validated to be accurate to reproduce some experimental results conducted in larger pores using similar nanofluidic devices [17]. The distance between the top and bottom amorphous silica layers is 2 nm which indicates the depth of the nanochannel in the fluidic device. To maintain the slit pore structure, the periodic boundary condition is only applied to the *x* and *y* directions of the model. The pore model is applied in the simulation box in the GCMC simulation and the fluid system box in the gauge-GEMC simulation.

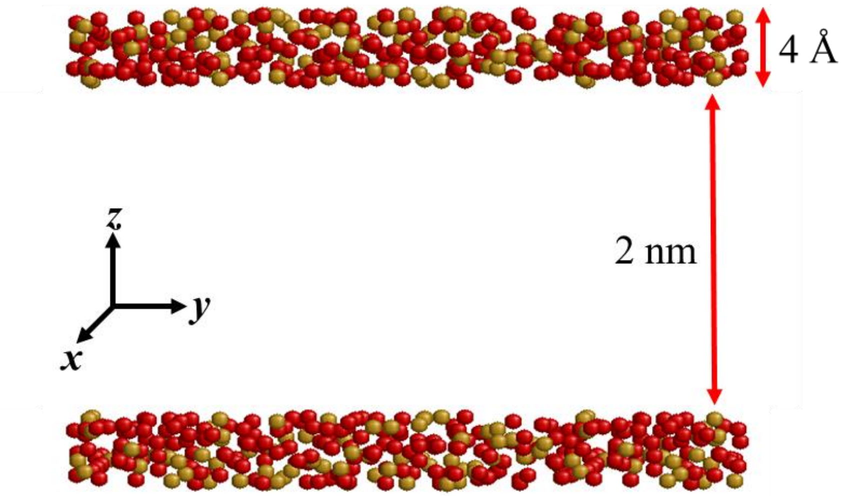

Figure 5: Amorphous silica 2 nm slit pore model. The thickness of the top and bottom layers is 4 Å. Red: Oxygen. Orange: Silicon.

2.3.3. Steele 10-4-3 Cylindrical Pore Model

For the study of the phase behavior of multicomponent mixtures in shale multi-scale models, the interactions between fluid molecules and the cylindrical pore boundary in Box III (see Fig. 3 in Section 2.1.3) are described by the Steele 10-4-3 potential [75]. A schematic of the Steele 10-4-3 cylindrical pore model is shown in Fig. 6. The Steele 10-4-3 cylindrical pore model is assumed to be formed by multiple-layer nanotubes (one-layer nanotube is a cylindrical tube that is made of one layer of graphite). The first layer of the nanotubes is separated from the second layer at a distance of $\alpha\Delta$ (Fig. 6c), where α represents an empirical adjustment ($\alpha = 0.61$) and Δ represents the regular distance between the graphite layers ($\Delta = 0.335$ nm). The rest layers (the layers except the first one) of the nanotubes are separated from each other in the regular distance Δ (Fig. 6d). The Steele 10-4-3 potential considers the rest layers as a continuum slab of material that has a uniform volumetric density ρ_s ($\rho_s = 114$ nm^{-3}).

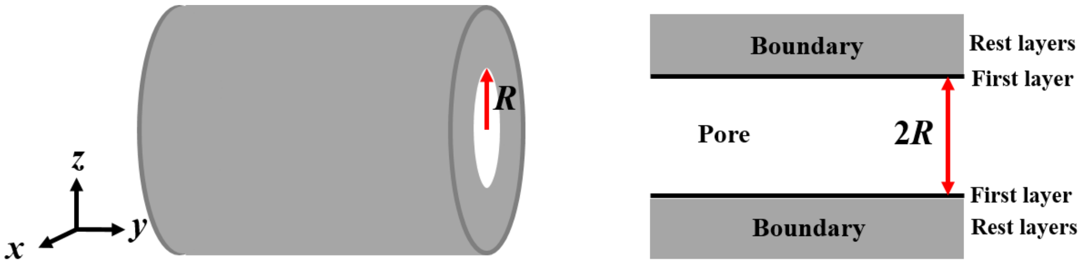

a) 3D view of the pore model

b) *y-z* cross-section view

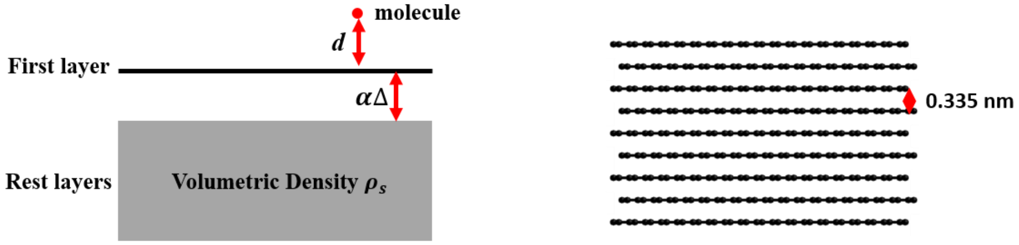

c) Magnified view of the boundary

d) Magnified view of rest layers

Figure 6: Schematic of the Steele 10-4-3 cylindrical pore model. a). 3D view of the pore model with a radius of R . b). *y-z* cross-section view of the model. c). A magnified view of the boundary. d). A magnified view of the rest layers.

By testing the confinement effect on the phase behavior of methane in 4 nm cylindrical pores using the Steele 10-4-3 model, one-layer nanotube model, and five-layer nanotube model (multi-walled nanotubes). The Steele 10-4-3 model has a similar confinement effect as the five-layer nanotube model (Fig. 7). However, instead of a sum over interactions with explicitly modeled the five-layer pore wall atoms, the interactions between the fluid molecules and the boundary can be presented by the simplified potential. The computational time is thus saved. The Steele 10-4-3 potential describes the interaction energy between fluid molecules and pore boundaries as follows:

$$U_{Steele}\left(d,\ R\right) = 2\pi\rho_s\Delta\sigma^2\epsilon[\psi_6(d,R,\sigma) - \psi_3(d,R,\sigma) - \frac{\sigma}{\Delta}\emptyset_3(d,R+\alpha\Delta,\sigma)], \tag{11}$$

$$\psi_n(d,R,\sigma) = 4\sqrt{\pi}\frac{\Gamma(n-0.5)}{\Gamma(n)}(\frac{\sigma}{R})^{2n-2}[1-(\frac{d}{R})^2]^{2-2n} \times$$
$$F[\frac{3-2n}{2},\frac{3-2n}{2};1;(\frac{d}{R})^2], \tag{12}$$

$$\emptyset_n(d,R,\sigma) = \frac{4\sqrt{\pi}}{2n-3}\frac{\Gamma(n-\frac{1}{2})}{\Gamma(n)}(\frac{\sigma}{R})^{2n-3}[1-(\frac{d}{R})^2]^{3-2n} \times$$
$$F[\frac{3-2n}{2},\frac{5-2n}{2};1;(\frac{d}{R})^2], \tag{13}$$

where U_{Steele} is the total interaction energy between fluid molecules and the pore boundary, d is the distance between the pore and the center of a molecule, R is the radius of the pore, ρ_s is the volumetric density of multi-layer graphite, Γ is the gamma function (Eq. 14), F is the hypergeometric function (Eq, 15), and the other parameters have the same definitions as the LJ potential. The gamma function and hypergeometric function can be computed as follows:

$$\Gamma(n) = (n-1)!, \tag{14}$$

$$F[a,b;c;z] = \sum_{n=0}^{\infty}\frac{(a)_n(b)_n}{(c)_n}\frac{z^n}{n!}, \tag{15}$$

where $q(n)$ has been defined as:

$$(q)_n = \begin{cases} 1 & n = 0 \\ q(q+1)\cdots(q+n-1) & n > 0 \end{cases}. \tag{16}$$

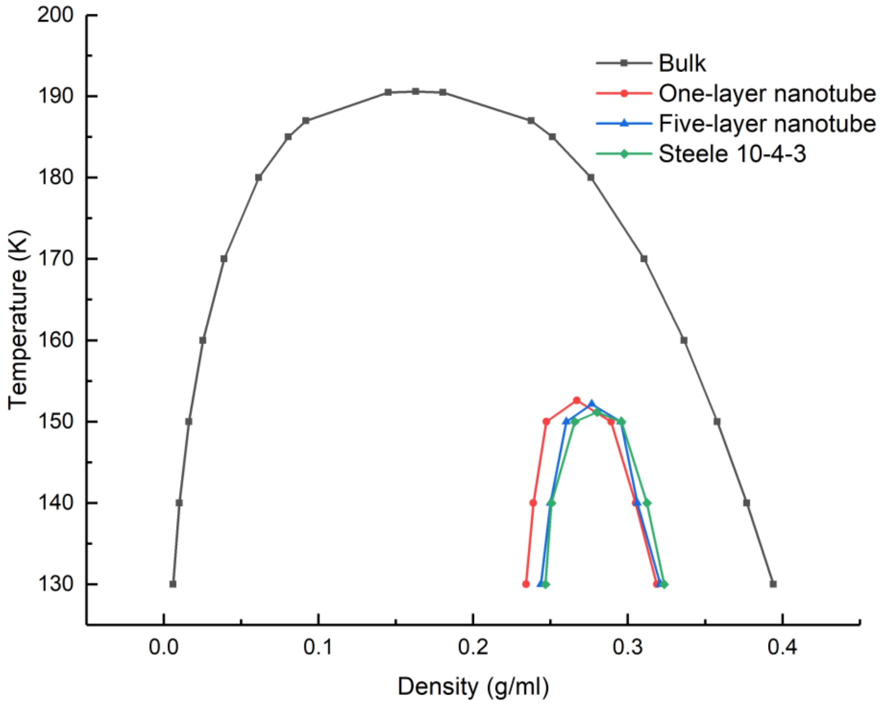

Figure 7: Temperature–density (*T*–*ρ*) diagrams of methane in 4 nm cylindrical pores of different models. The black, red, blue, and green refer to the bulk, one-layer nanotube model, five-layer nanotube model, and the Steele 10-4-3 model, respectively. Adapted from [80].

3. RESULTS AND DISCUSSIONS*[†]

3.1. Single-Component Fluids in Single-pore Models

3.1.1. Phase Behavior of Methane in 4–10 nm Cylindrical Pores

The gauge-GEMC simulation is applied for investigating the phase behavior of methane in cylindrical pores of different sizes. For each pore size, simulations are performed at multiple temperatures from 130 K to 190 K. At each temperature, the gauge-GEMC simulation includes a series of cases that cover a range of numbers of molecules (Fig. 8). It should be noted that, for each case, the system is defined with a constant number of molecules (N), total volume (V), and temperature (T). Further, two million Monte Carlo steps [53] are performed for the system to reach equilibrium.

---

[*] Part of this chapter is reprinted with permission from "Molecular Simulation of the Constant Composition Expansion Experiment in Shale Multi-Scale Systems" by Ran Bi and Hadi Nasrabadi, 2019. *Fluid Phase Equilibria*, 495, 59-68, Copyright [2019] by Elsevier B.V.

[†] Part of this chapter is reprinted with permission from "Molecular Simulation of the Pore Size Distribution Effect on Phase Behavior of Methane Confined in Nanopores" by Bikai Jin, Ran Bi, and Hadi Nasrabadi, 2017. *Fluid Phase Equilibria*, 452, 94-102, Copyright [2017] by Elsevier B.V.

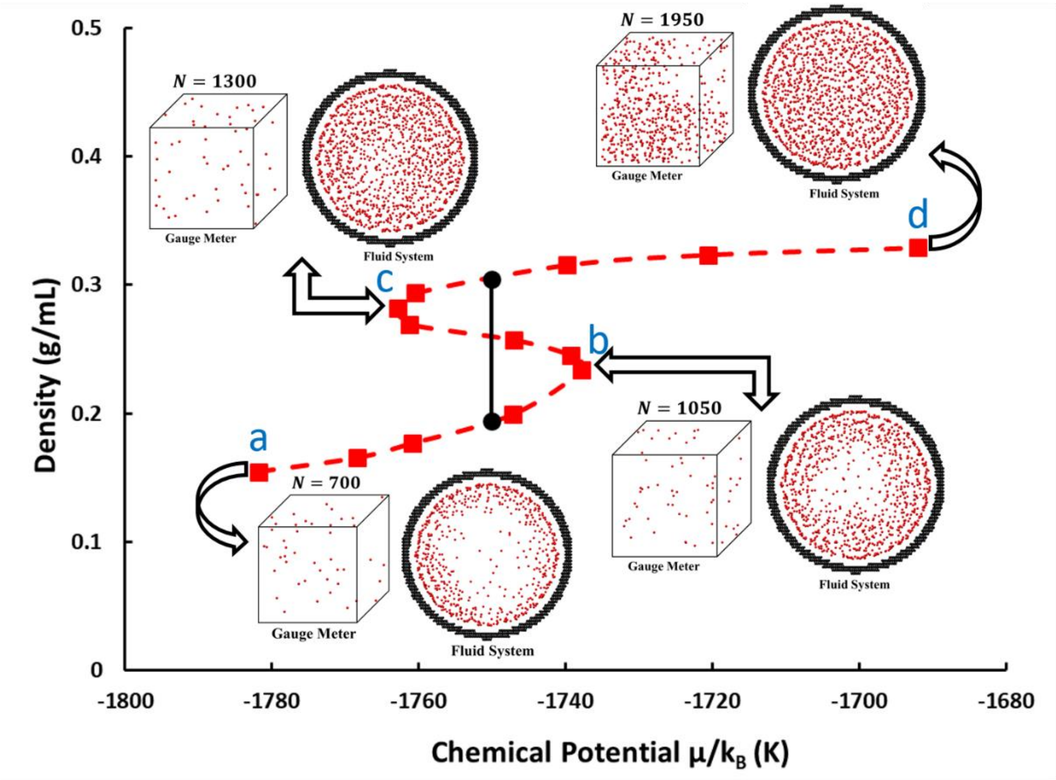

Figure 8: An example of the chemical potential–density relation for methane in a 6 nm cylindrical pore at $T = 160$ K from the gauge-GEMC simulations. Red squares represent the density of methane in the fluid system box at various chemical potentials. Black circles are the phase equilibrium points computed by the Maxwell equal area rule. Points a and d demonstrate the vapor and liquid stable state, respectively. Points c and d are in meta-stable states. Red and black balls in the simulation boxes are methane and pore boundary (graphite), respectively.

At each temperature, a chemical potential–density (μ–ρ) diagram (also known as the van der Waals loop) can be generated by running the designed series of cases (Fig. 8). The van der Waals loop contains stable points and meta-stable points. Phase equilibrium points can be computed following the thermodynamic integration of the Maxwell equal area rule [81]. Once the vapor and liquid densities at the equilibrium are obtained, they are used to construct the temperature–density (T–ρ) diagram (Fig. 9). The critical points (critical temperature and density) are extrapolated from the simulation results at lower temperatures by the rectilinear diameter law [82,83] and density scaling law [84].

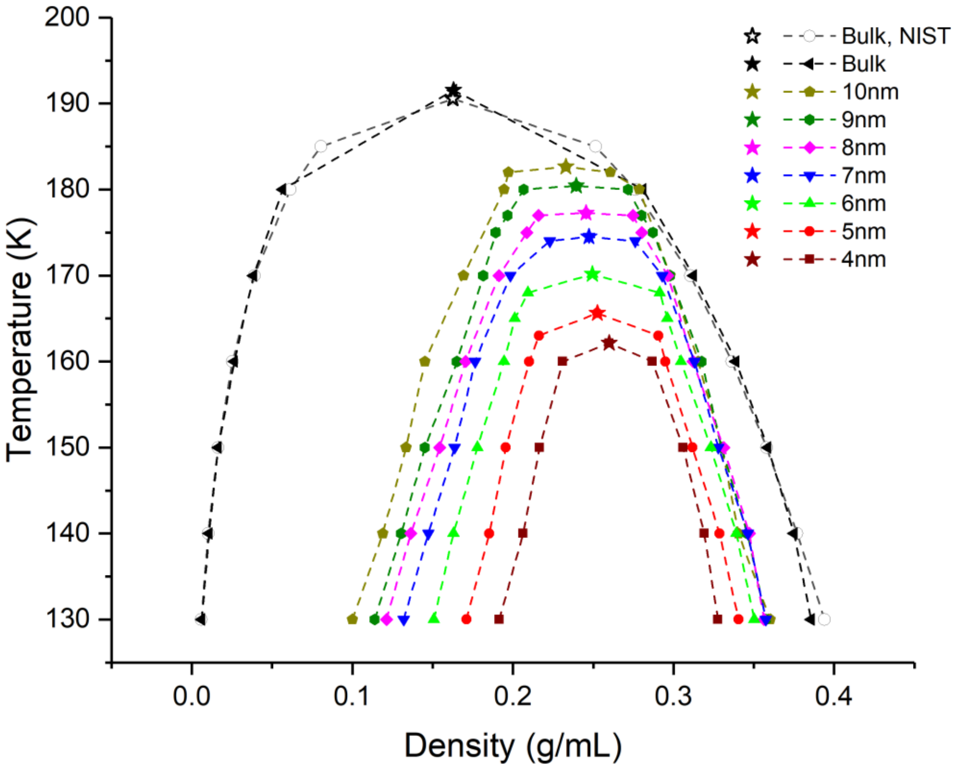

Figure 9: Temperature–density (T–ρ) diagrams of methane in cylindrical models with different diameters. Adapted from [1].

First, the accuracy of the set-up in the gauge-GEMC method is tested in the bulk condition. In the bulk condition, there is no pore boundary involved in the fluid system box and further, the fluid system box is in the 3D periodic boundary condition. Our simulation can generate results as accurate as the laboratory results from the National Institute of Standards and Technology (NIST). Our results (represented as black triangles) from the simulation match the results (represented as empty circles) from NIST in Fig. 9.

Additionally, we extend the work to confined systems that contain the multi-layer graphite cylindrical pore models (see Section 2.3.1) with varying diameters in the range of 4–10 nm in the fluid system box. By repeating the mentioned tests for each pore size, phase diagrams are computed, as shown in Fig. 9. It is clear that the smaller the pores are, the more the temperature–density diagrams shrink. In comparison with the bulk condition, the critical temperature is reduced, while critical density increases in nanopores. The critical temperature in the 4 nm pore that deviates the most from the values in the bulk condition is reduced by around 15%. The increase in the critical density is the consequence of the dramatic increase in the vapor density and slight decrease in the liquid density at equilibrium. As the diameter of the pore increases, the phase diagram approaches its bulk values. The above confinement effects have similar trends as observed in other works [18,50,62].

An example of the density profiles of methane at 130 K in the mentioned nanopores is shown in Fig. 10. We measure the mass densities as a function of the distance from the pore surface (r). We divide the entire distance into series intervals (the width of each interval $\Delta r = 0.05$ nm) and count how many molecules fall into each interval. As the figure shows, for both liquid and vapor phases, there are two obvious methane adsorbed layers near the pore boundary at around $r = \sigma_{methane}$ and $2\sigma_{methane}$, where r is defined to be zero at the pore surface. The densities of the first adsorbed layers in both phases are the same, while the density of the second layer in the liquid phase is larger than that in the vapor phase. As the distance increases, the confinement effect by the wall decreases, and both the liquid and vapor densities gradually approach their bulk values.

There are some transition layers before the liquid and vapor densities reach their bulk values. It should be noted that in comparison with small pores (e.g., 4 nm pore), large pores (e.g., 10 nm pore) contain a larger free region in their center, but the same molecular distributions near the pore boundary.

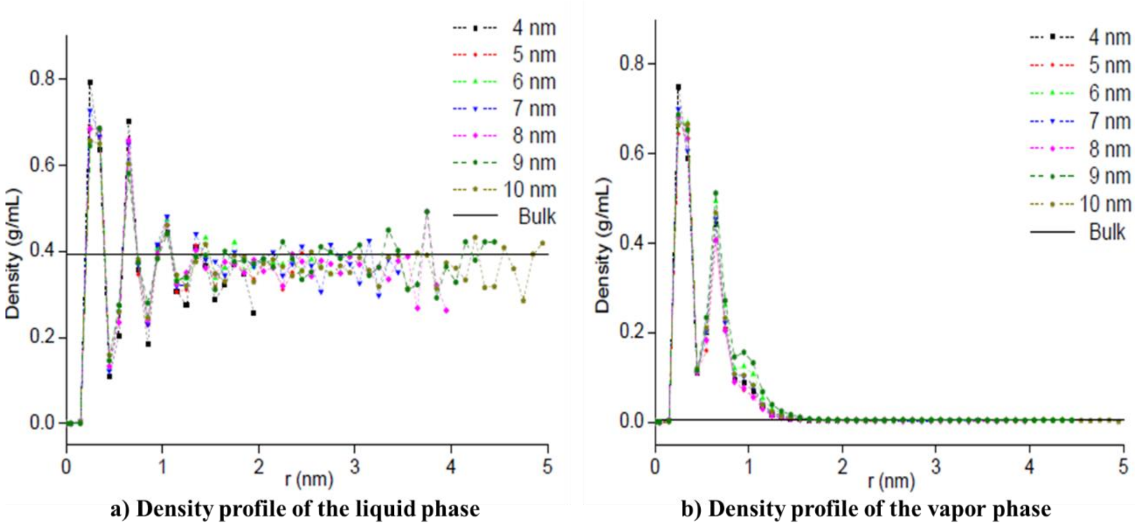

a) Density profile of the liquid phase

b) Density profile of the vapor phase

Figure 10: Density profile of methane in cylindrical models with different diameters at 130 K. The a) liquid and b) vapor phase densities as a function of the distance r. Adapted from [1].

Pressure–temperature diagrams (Fig. 11) are generated from additional GCMC simulations (two million Monte Carlo steps) with the obtained chemical potentials at equilibrium states as imposed chemical potentials. As explained in Section 2.1.2, the additional GCMC simulations are performed in the bulk condition. In comparison with the bulk condition, the critical pressure is reduced in the nanopores. The smaller the pores are, the lower the pressure–temperature diagrams go. As a result, the saturation pressures at different temperatures are suppressed, compared with the value in the bulk condition.

Overall, the saturation and critical pressure in the 4 nm pore, as the most confined condition, deviates the most from the values in the bulk condition. Compared with the bulk condition, saturation pressures in the 4 nm pore reduce 48–60% at various temperatures and the critical pressure reduces by around 80%.

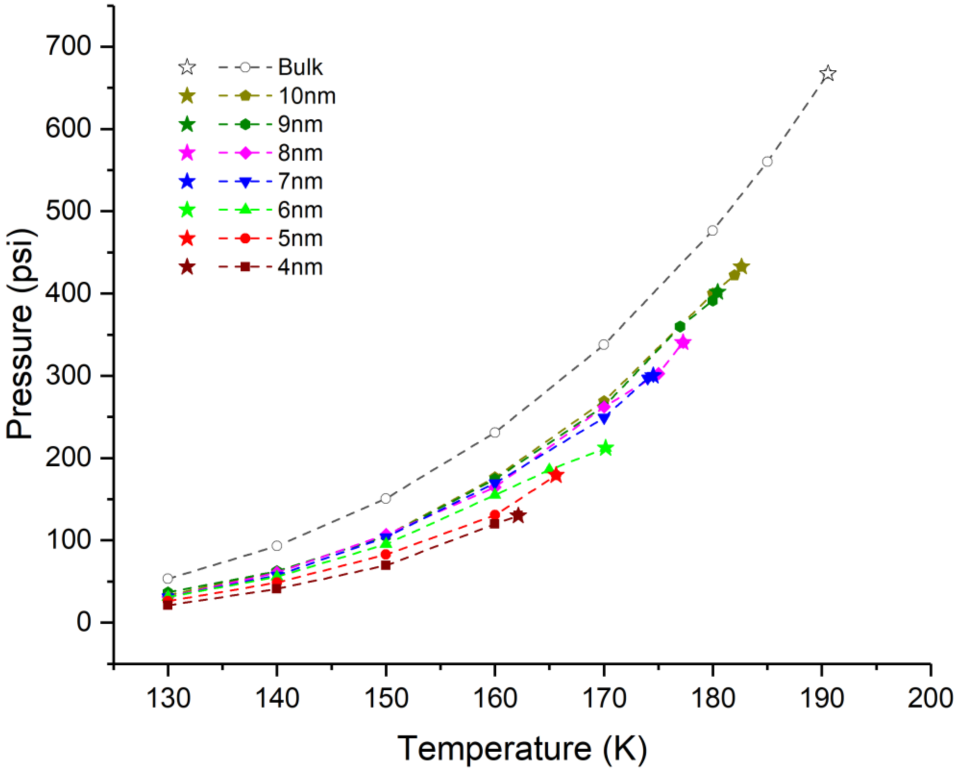

Figure 11: Pressure–temperature (*P*–*T*) diagrams of methane in cylindrical models with different diameters.

3.1.2. Adsorption Isotherms and Hysteresis Effect of n-Butane in 2 nm Slit Pore

Adsorption and desorption of hydrocarbons in nanopores have been conducted in many experimental techniques (e.g., the lab-on-a-chip). Hysteresis has been observed between the phase transition pressures measured during the adsorption and desorption processes. Recently, Yang et al. [17] measured the transition pressures of n-butane in 4 nm, 10 nm, and 50 nm using the lab-on-a-chip technique. In this study, we use the molecular simulation to further investigate the phase behavior of n-butane in a smaller (2 nm) pore using the amorphous silica slit pore model (see Fig. 5 in Section 2.3.2). We perform the GCMC simulations to model the adsorption and desorption processes that are conducted in the lab-on-a-chip experiments and investigate the hysteresis caused by the confinement effect.

The GCMC simulations are performed at a temperature of 298.15 K with a series of cases that cover a wide range of chemical potentials (μ_{nC4}/k_B is from -3000 to -2400 K). For each case, the system is specified with constant chemical potential (μ), volume (V), and temperature (T). By modeling the cases with various chemical potentials, we obtain the chemical potentials at which phase transitions happen in the adsorption and desorption processes and subsequently use these to compute the phase transition pressures. In this work, all the simulations (adsorption, desorption, and phase transition pressure computations) are designed with four million Monte Carlo steps. Properties in the last one million steps are averaged to generate results.

In the study of the adsorption, we initially designed the simulations using cases with specified chemical potentials (μ_{nC4}/k_B) from -3000 to -2400 K, with a large interval ($\Delta\mu_{nC4}/k_B = 50$ K) between cases. This helps us to quickly estimate a small range of chemical potentials at which the condensation of the n-butane gas will happen. Further, another series of refined cases ($\Delta\mu_{nC4}/k_B = 5$ K) are designed with chemical potentials within the small range to find the moment at which condensation happens. All the cases in the adsorption study are initialized with empty occupancies of n-butane in the system. In terms of the desorption study, simulations are designed inversely with μ_{nC4}/k_B from -2400 to -3000 K and decrement rates of 50 K in original cases and 5 K in refined cases. Unlike the adsorption study, systems in the desorption study are initialized with the final configuration of the case with the largest chemical potential in the adsorption branch (the initial occupancy of n-butane in the desorption study is the final configuration of the adsorption case with $\mu_{nC4}/k_B =$ -2400 K).

From the chemical potential-density relationship (Fig. 12) obtained from the simulations, we find the chemical potentials at which phase transitions occur in both the adsorption and desorption branches. The gaseous n-butane starts to condense at $\mu_{nC4}/k_B =$ -2679.44 K in the adsorption study while the liquid n-butane vaporizes during the desorption process at $\mu_{nC4}/k_B =$ -2809.53 K. Two extra GCMC simulations in the bulk condition at specified chemical potentials of -2679.44 and -2809.53 K are performed to compute the condensation and vaporization pressures. The results of the phase transition pressures are tabulated in Table 3. The condensation and vaporization pressures of n-butane in the 2 nm channel are 26.66 and 16.87 psi, respectively. A strong hysteresis effect is observed. The pressure at which liquid n-butane vaporizes is 36.7% lower than the pressure at which vapor n-butane condenses. The hysteresis between the phase transition pressures is 9.79 psi.

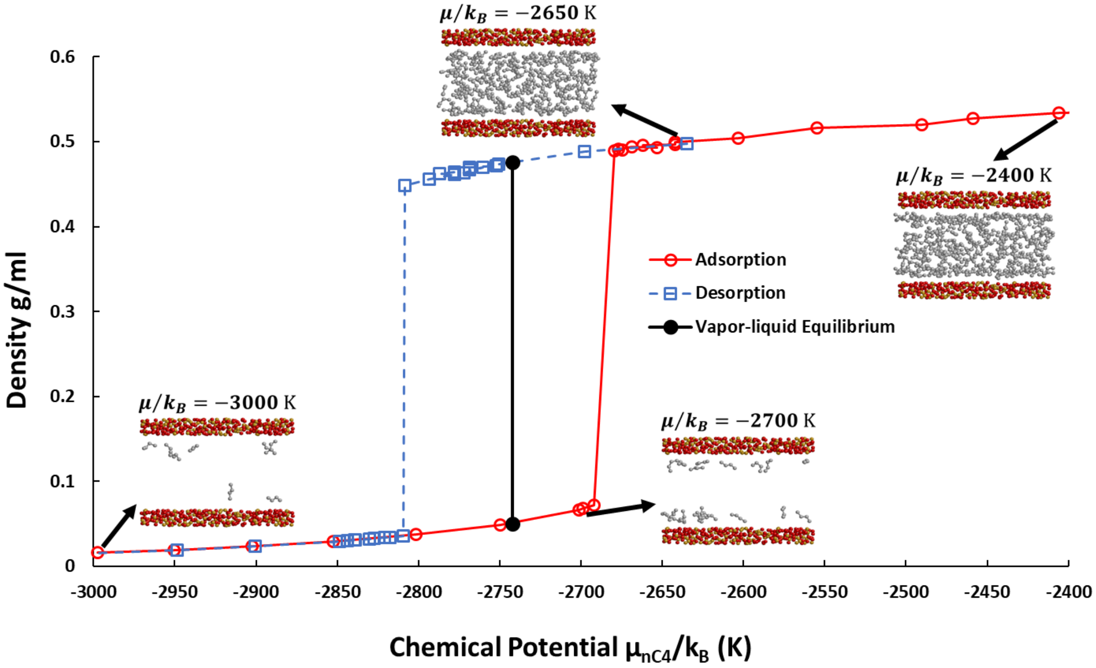

Figure 12: The chemical potential–density ($\mu/k_B - \rho$) relationship from the adsorption and desorption simulations of n-butane in the 2 nm slit pore channel at 298.15 K (25°C) using the GCMC simulations. Empty red circles and empty blue squares represent the density of n-butane in the fluid system box at various chemical potentials in the adsorption and desorption branches, respectively. Full black circles are the phase equilibrium points computed by the gauge-GEMC simulation. Grey particles in the pore are n-butane molecules. Red and orange balls are the oxygen and silicon in the pore boundary, respectively.

Table 3: Phase transition pressures of n-butane in the 2 nm channel at 298.15 K (25°C).

	Chemical Potential (K)	**Phase Transition Pressure (psi)**
Adsorption	-2679.44	26.66
Desorption	-2809.53	16.87

We also use the gauge-GEMC simulations to calculate the saturation pressure of n-butane at vapor–liquid equilibrium in the 2 nm amorphous silica slit pore at 298.15 K. We design the simulations with a series of cases with the numbers of molecules ranging from 10 to 200 to generate the chemical potential–density relationship (Fig. 13). The chemical potential at the equilibrium determined by the Maxwell equal area rule [81] is -2741.96 K. Similar to the GCMC simulations, the chemical potential (-2741.96 K) at vapor–liquid equilibrium is then used to run a GCMC simulation in the bulk condition to calculate the pressure. We obtain a saturation pressure of 21.50 psi for n-butane in the 2 nm channel at vapor–liquid equilibrium. The saturation pressure of n-butane in the 2 nm channel is suppressed by 38.82% compared to that of 35.29 psi for n-butane in the bulk condition at 298.15 K because of the confinement effect.

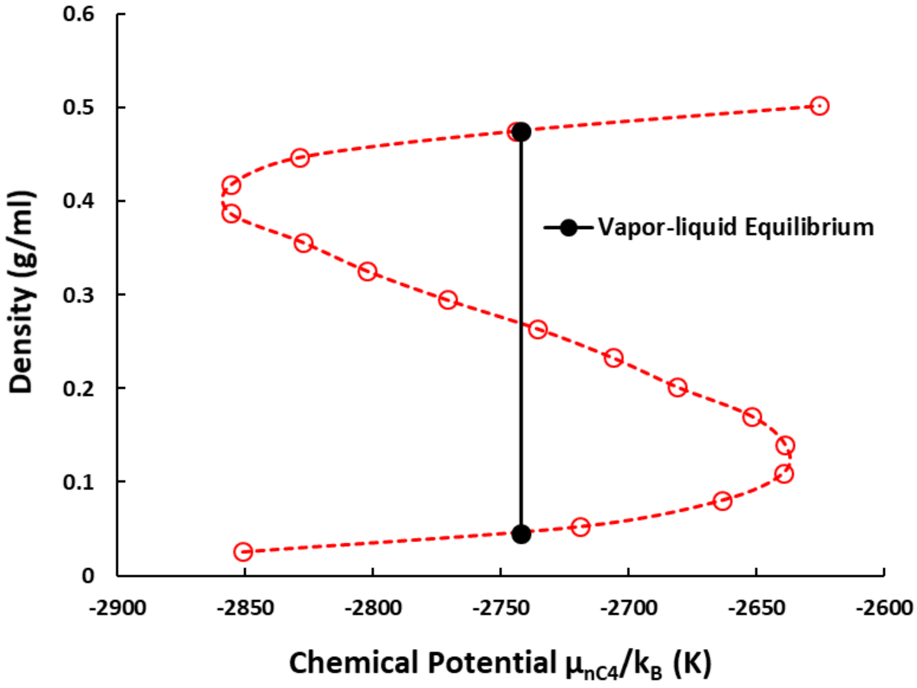

Figure 13: The chemical potential–density (μ/k_B–ρ) relationship from the gauge-GEMC simulations of n-butane in the 2 nm slit pore channel at 298.15 K (25°C). Full black circles indicate the vapor–liquid equilibrium points which are calculated by using the Maxwell equal area rule.

3.2. The Effect of the Pore Size Distribution

In this section, we study the pore size distribution (PSD) effect on confined fluid phase behavior for an Eagle Ford shale rock sample. Eagle Ford shale is a sedimentary formation with a large amount of oil and natural gas in South Texas. It was one of the most active targets for unconventional production in the U.S. Based on the PSD data of Eagle Ford shale obtained from mercury intrusion [9], several pore sizes are chosen to represent the Eagle Ford shale sample (Fig. 14). The selection of representative pore sizes mainly considers pores that have a relatively high volume fraction and phase behavior characteristics that deviate significantly from bulk conditions. Once the representative pore sizes of the PSD are chosen, the volume fraction of each of them can be determined by matching the area of pore sizes and volume fraction plot of the Eagle Ford sample. The measured Eagle Ford PSD from mercury intrusion [9], representative pore sizes, and volume contribution of each pore are shown in Fig. 14. Pore sizes of 4, 5, 6, 8, and 13 nm are picked to represent pore sizes of 3 to 4 nm, 4 to 5 nm, 5 to 6.25 nm, 6.25 to 9 nm, and 9 to 30 nm, respectively, in the Eagle Ford sample. Due to the small volume contribution and highly time-consuming requirements of molecular simulation, we did not consider pores that had diameters more than 30 nm. Previous studies [29,33] have shown that the confinement effect becomes negligible for such pore sizes. The final PSD model (Fig. 15) for this Eagle Ford sample includes five pores independently arrayed in parallel with 1D periodic boundary conditions in the *z*-direction. Pores are separated far enough, which means that fluid molecules in a given pore are not affected by boundary molecules in neighboring pores. The volume fraction of the pore size is defined as the summation of the pore volume with the same diameter divided by the total system volume.

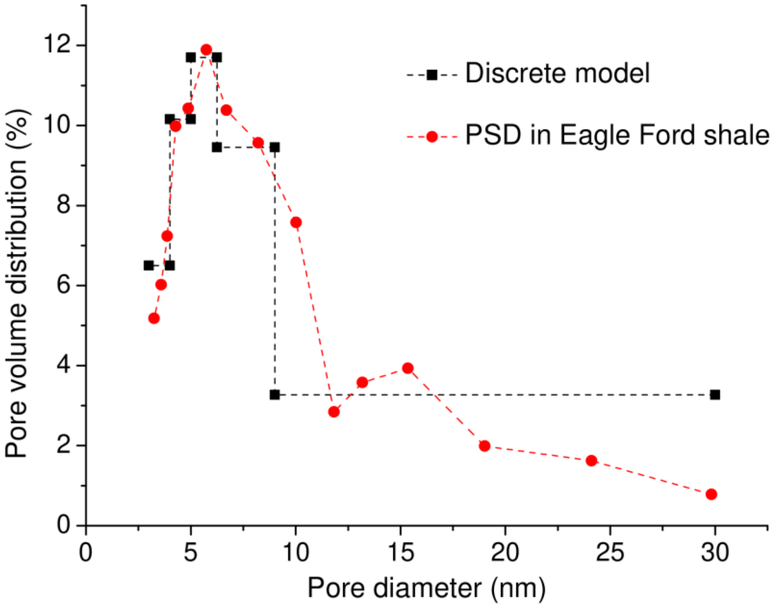

Figure 14: Normalized pore size distribution (PSD) of the Eagle Ford sample and discrete model. Reprinted from [1].

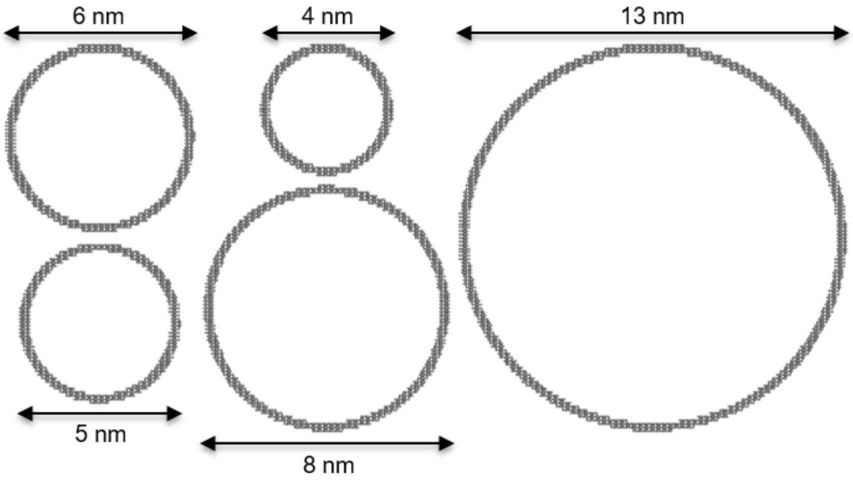

Figure 15: The pore size distribution model of the Eagle Ford sample.

The volume of a system is the summation of the volume of each pore; further, the system density is an average property for the entire space of the pores. During the simulation, the Eagle Ford model is treated as a "black box." The phase definitions and equilibrium properties only depend on the thermodynamic relationship between the chemical potential and system density (Fig. 16). We further construct the temperature–density diagram of methane in the Eagle Ford PSD model in Fig. 17 and compare the solutions (both the chemical potential–density and temperature–density diagrams) with those of methane in cylindrical single-pore models. The phase diagram of methane in this Eagle Ford sample is close to that in a 10 nm cylindrical single-pore model. It can be inferred that this Eagle Ford sample has an equivalent confinement effect similar to that of a single pore of 10 nm. Simulation results of the 10 nm single-pore model can be used to estimate the phase behavior and related reservoir fluid characteristics of this Eagle Ford sample. We do not claim that it is possible to find an "effective pore radius" that can be used to model the confined phase behavior for any rock sample with a wide PSD. The existence of such a pore radius or its value requires a case-by-case analysis.

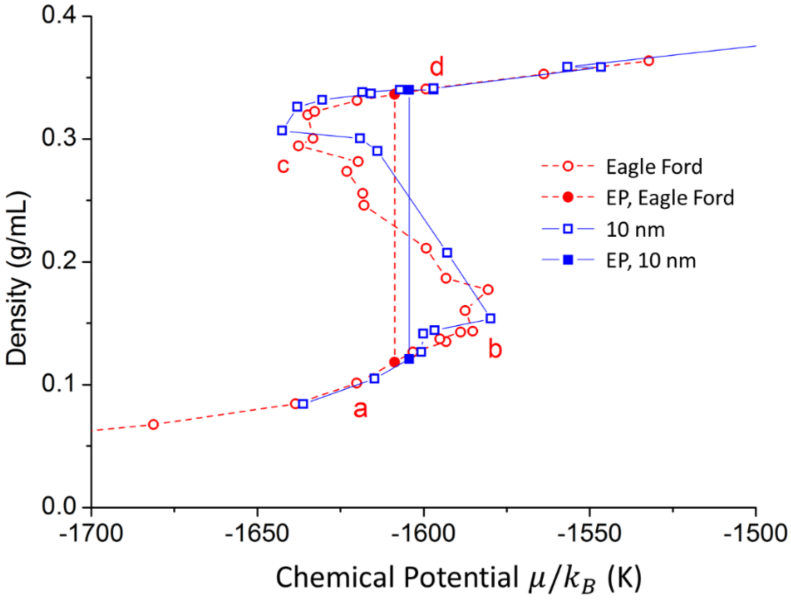

Figure 16: The chemical potential–density (μ/k_B–ρ) diagrams for methane in the Eagle Ford pore model and a 10 nm cylindrical single-pore model. EP represents equilibrium points. Adapted from [1].

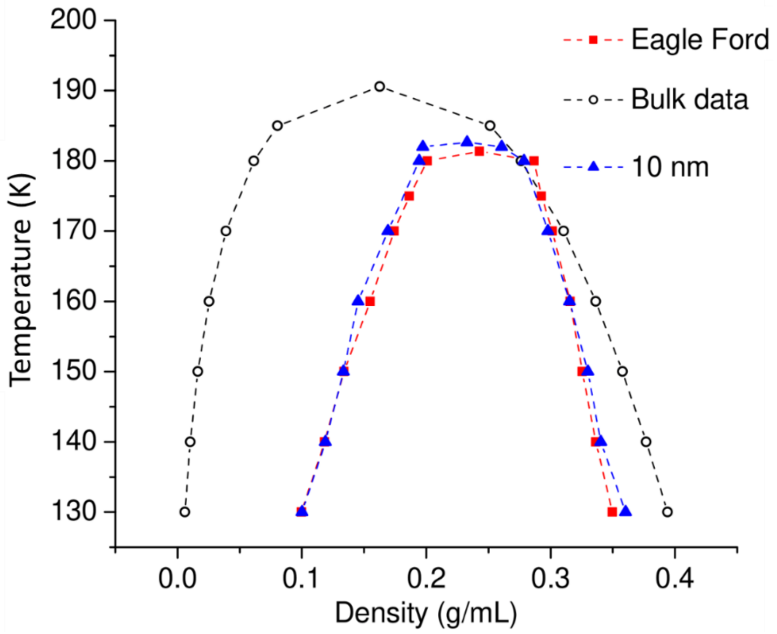

Figure 17: Temperature–density (T–ρ) diagrams for methane in the Eagle Ford pore model and a 10 nm cylindrical single-pore model. Adapted from [1].

The methane molecular distribution is studied based on the final configurations when the systems are stable (Fig. 18). From Fig. 18a to Fig. 18d, the number of methane molecules increases. As the figures show, adsorption layers in all the pores are formed at the very beginning. Thereafter, methane in the smallest pores will condense first, while larger pores are still in the vapor phase. Methane in the largest pore will vaporize first, while smaller pores are still in the liquid phase. Take Fig. 18a as an example, methane in the pore of 4 nm has condensed, while the fluids in other pores are gaseous. In Fig. 18c, methane in the pore of 13 nm starts to vaporize, while the fluids in other pores are still liquid.

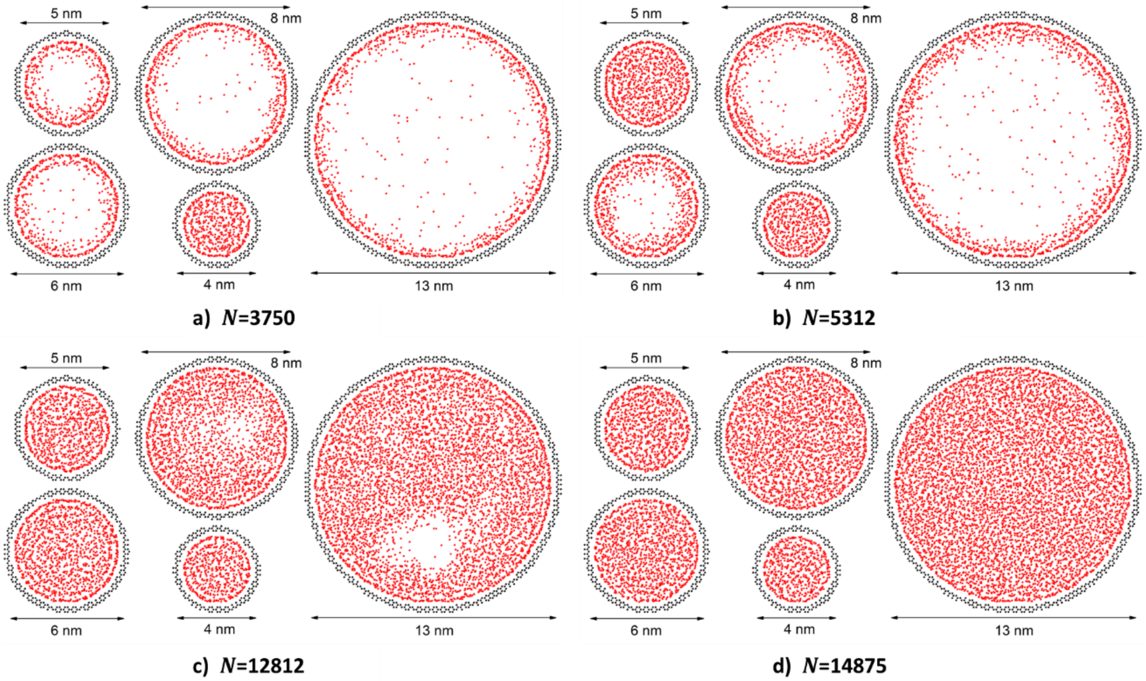

a) *N*=3750

b) *N*=5312

c) *N*=12812

d) *N*=14875

Figure 18: Top views of the methane molecular distribution in the Eagle Ford PSD model at 140 K. Black: Graphite model. Red: Methane molecules. The number of methane molecules is given at the bottom of each graph. Adapted from [1].

3.3. Multicomponent Fluids in Shale Multi-Scale Models

In this section, we demonstrate our work for investigating the phase behavior of multicomponent fluids in shale multi-scale models using the modified NPT-GEMC method (see Section 2.1.3). We simulate the CCE experiment which is a typical PVT test to investigate bulk fluid phase behaviors. This is in an isothermal condition and usually performed at the reservoir temperature. The CCE test starts from a pressure higher than the saturation pressure. As the pressure gradually decreases, the volume expands at constant composition. The bubble point or dew point pressure can be measured and fluid properties, which change with pressure, can be obtained from the test. For all the cases in this section, at least four million Monte Carlo steps are run for the system to reach equilibrium and another two–four million Monte Carlo steps are used to generate configurations and evaluate average properties.

Theoretically, at the bubble point and dew point of a system, the phase volume ratios (V_{liquid}/V_{vapor} and V_{vapor}/V_{liquid}, respectively) are infinite. Since simulation boxes have a minimum size limitation ($2 \times r_{cutoff}$), an infinite total number of molecules will be needed. However, from our research, we find the NPT-GEMC simulation is good enough to detect phase coexistences using a limited number of molecules when the conditions (P and T) of the simulations are very close to the bubble and dew points. The more molecules we use, the closer we can get to the saturation point. Therefore, it is sufficient to estimate the bubble or dew points by using several tests close to the saturation line in the P–T diagram.

3.3.1. Validations of the Modified NPT-GEMC Simulation

The validation of the modified NPT-GEMC simulation is conducted to verify our codes and simulation settings. During the validation, we change the confined boundary in Box III in the multi-scale model (see Fig. 3 in Section 2.1.3) to the bulk condition by deleting the nanopore boundary and applying a 3D periodic boundary condition to the simulation box. By doing this, the whole system is in the bulk condition, so that results from PR EOS can be used as references to validate our results.

We first reproduce pressure–composition diagrams of a binary mixture with 70% methane and 30% ethane composition in Mccain [92]. The NPT-GEMC simulations are performed with the feeding fluid (70% methane and 30% ethane binary mixture) at various pressures and temperatures. The simulation results of pressure–composition diagrams are presented and compared with the data in the reference in Fig. 19a. Further, the pressure–temperature (*P*–*T*) diagram of the same binary mixture is conducted using the NPT-GEMC method. During the process, several simulations are conducted with different temperatures at each specified pressure. The bubble and dew points are predicted when the state of fluid turns from the single- to two-phase state. The results are showing in Fig. 19b. Overall, our simulation results highly agree with the data in reference [92].

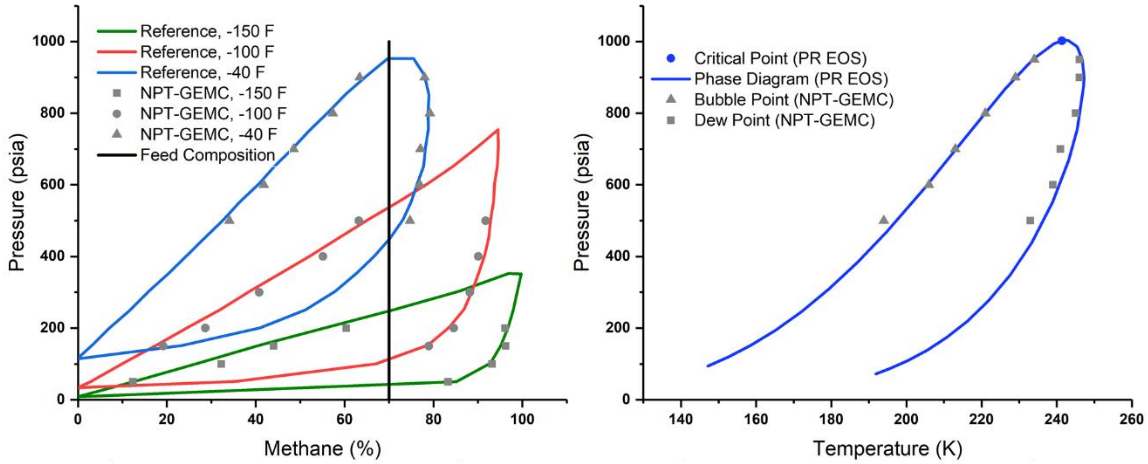

a) Pressure-composition Diagrams

b) Pressure-temperature Diagram

Figure 19: Validation of the NPT-GEMC simulation using the 70% methane and 30% ethane mixture. a). Pressure–composition diagrams. The blue, red, and green lines refer to the data from the reference at -150°F, -100°F, and -40°F, respectively. The squares, diamonds, and triangles indicate the simulation results at corresponding temperatures, respectively. The black line is the initial feed composition before the flash calculations. b). *P*–*T* phase diagram. The blue circle and line refer to the critical point and phase envelope calculated from PR EOS. The gray triangles and squares are the bubble and dew points calculated from NPT-GEMC simulations, respectively. Adapted from [80].

To test the algorithm with a more complex fluid, we regenerate the phase envelope of an eight-component synthetic mixture with a composition listed in Table 4. Because the molecular simulation can only handle an integer number of molecules, the composition of the mixture in the simulation is slightly different from the reported composition. However, the difference between the mole fractions, as shown in Table 4, is less than 0.001 for each species. The phase envelope reproduced from the modified NPT-GEMC simulations is shown in Fig. 20, and it agrees well with the PR EOS results.

Table 4: The eight-component synthetic mixture and number of molecules of each species used in the simulation. Adapted from [80].

	Original	Simulation		Mole fraction difference
Component	**Mole fraction**	**Num. of molecules**	**Mole fraction**	
CO_2	0.0254	100	0.025	0.00041
N_2	0.00514	21	0.0052	0.00011
C_1	0.66225	2649	0.6621	0.00017
C_2	0.14793	592	0.148	0.00003
C_3	0.10171	407	0.1017	0.00001
C_4	0.03927	157	0.0392	0.00003
C_5	0.01119	45	0.0112	0.00006
C_6	0.00747	30	0.0075	0.00003
Total	1	4001	1	

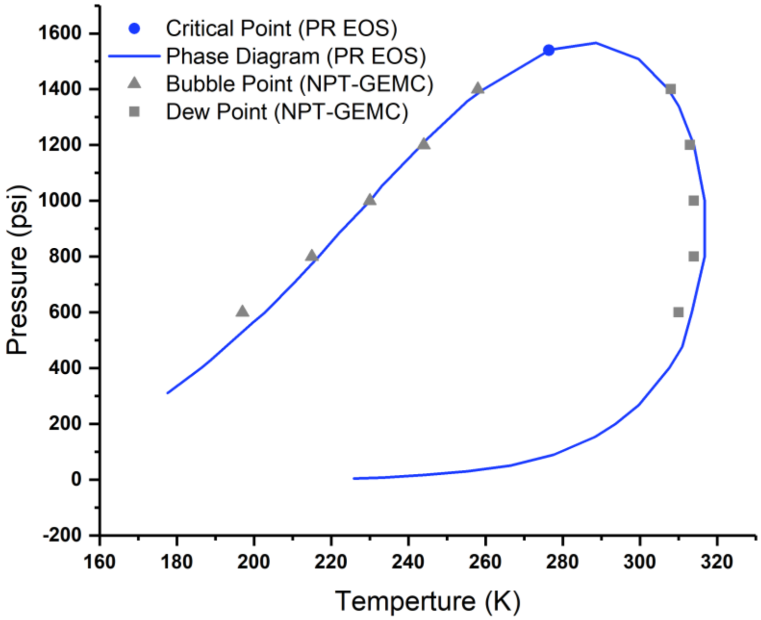

Figure 20: The reproduced phase envelope of the multi-component mixture. The blue circle and line refer to the critical point and phase envelope from the PR EOS, respectively. The gray triangles and squares are the bubble and dew points from the NPT-GEMC simulations, respectively. Adapted from [80].

3.3.2. Methane/Ethane Mixture in the Multi-Scale Model

The modified NPT-GEMC method is used to simulate the CCE experiments at a temperature of 220 K with pressures ranging from 1,000 psi to 500 psi. This binary mixture has 70% methane and 30% ethane. We use 2,700 molecules (1,890 methane and 810 ethane) in the simulation. The confined region is built using a nanopore with a diameter of 4 nm. The volume fraction of the confined region is 30%. The bulk region will expand when we decrease the pressure. However, the volume of the confined region is kept constant at various pressures. The compositions of the fluids in each phase and scale at different pressures are shown in Fig. 21.

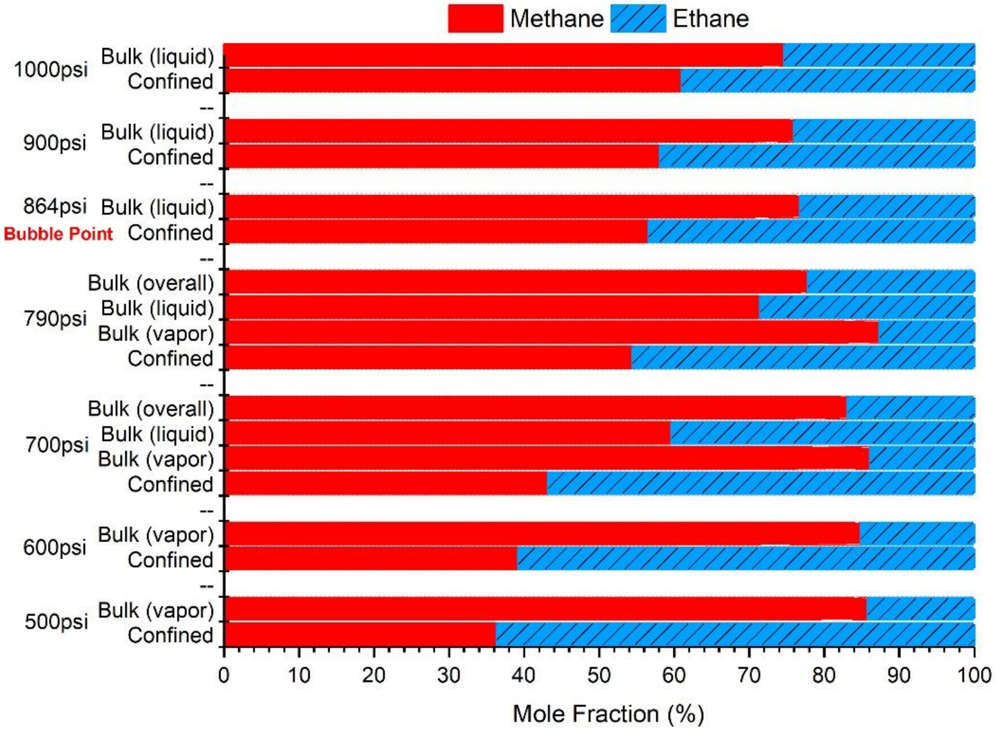

Figure 21: Methane/ethane mixture: The compositions of the fluids for each phase in bulk and confined regions at 220 K. The red and blue bars with slashes are methane and ethane, respectively. The bubble point pressure is 864 psi. Reprinted from [80].

As Fig. 21 shows, compared with the original mole fraction of methane (70%), the mole fraction of methane becomes higher in the bulk region and lower in the confined region. At 1,000 psi, the mole fractions of methane in the bulk and confined regions are 74.7% and 61.0%, respectively. Therefore, the composition of the fluid in the bulk region becomes lighter than the original composition. As the pressure decreases, this difference increases. Consequently, the first bubble in the bulk region appears at a pressure of 864 psi. The bubble point pressure in the shale multi-scale model is around 74 psi (9.3%) higher in comparison with the bubble point pressure (790.35 psi) of the same fluid in a conventional reservoir condition.

By counting the number of molecules of each species in the confined and bulk regions, we find the amount of methane in the nanopore keeps decreasing during the whole process of the CCE simulation. When the pressure is above the bubble point pressure (no vapor phase in the bulk region), the amount of methane in the bulk liquid phase increases as the pressure decreases. Once the pressure drops below the bubble point pressure, most of the methane molecules move to the vapor phase in the bulk region. In contrast to methane, the amount of ethane in the confined region keeps increasing during the CCE simulation. As the pressure decreases, the ethane molecules in the bulk liquid phase move not only to the vapor phase in the bulk region but also nanopore in the confined region. At the lowest pressure of the CCE experiment, around 16.6% of methane and 67.8% of ethane remains confined in the nanopore, that is, 83.4% of methane molecules and 32.2% of ethane molecules are in the vapor phase in the bulk region. At each pressure, the distributions of methane and ethane in the entire system, indicating the number of methane/ethane molecules that are present in a certain region at specific pressures, are demonstrated in Figs. 22a and 22b, respectively.

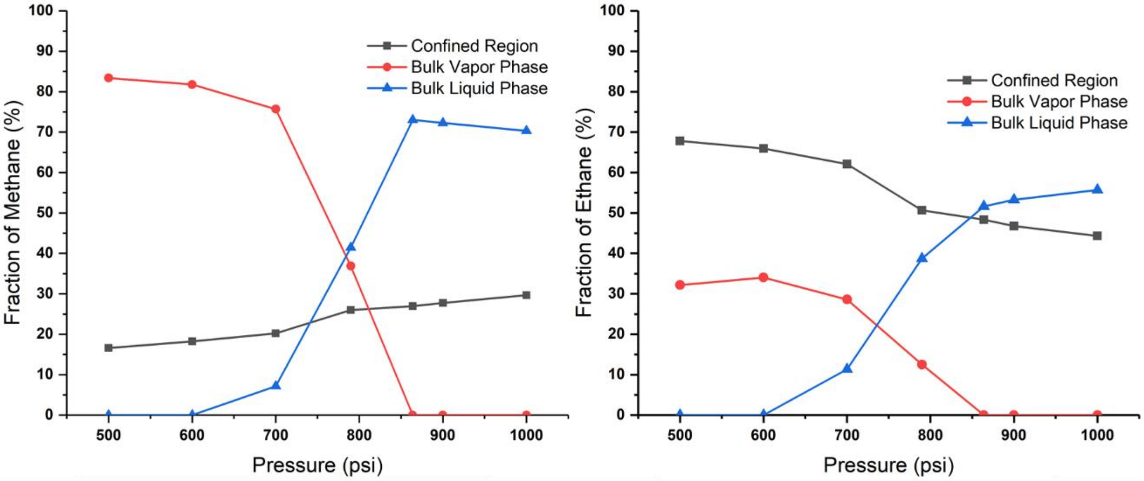

a) Methane Distribution in the System

b) Ethane Distribution in the System

Figure 22: Methane/ethane mixture: The distribution of methane and ethane. The black squares indicate the confined region. The red circles and blue triangles represent the vapor and liquid phases in the bulk region, respectively.

The results of the CCE experiment from the NPT-GEMC simulation, including the relative volume, liquid saturation, and fluid densities, are compared with the CCE results, which are calculated by the PR EOS, assuming conventional reservoir conditions in Figs. 23a, 23b, and 23c, respectively. Because the bubble point pressure increases, the relative volume in the shale multi-scale model starts to rise at a higher pressure. The rates of the increases in both conditions, however, are not very different. Compared with the liquid saturation in the conventional reservoir condition, that is bulk condition, the drop in the liquid saturation in the shale multi-scale model starts at a higher pressure with a slightly steeper slope. Both the gas and liquid densities in the bulk region of the shale multi-scale model are less than those calculated in the conventional reservoir condition. The difference in liquid density is more substantial when the pressure is above the bubble point.

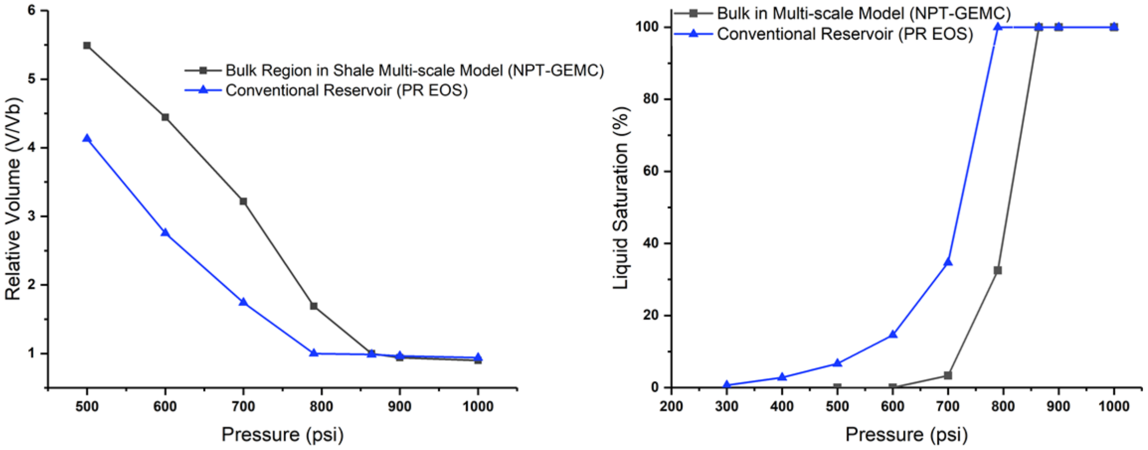

a) Relative Volume **b) Liquid Saturation**

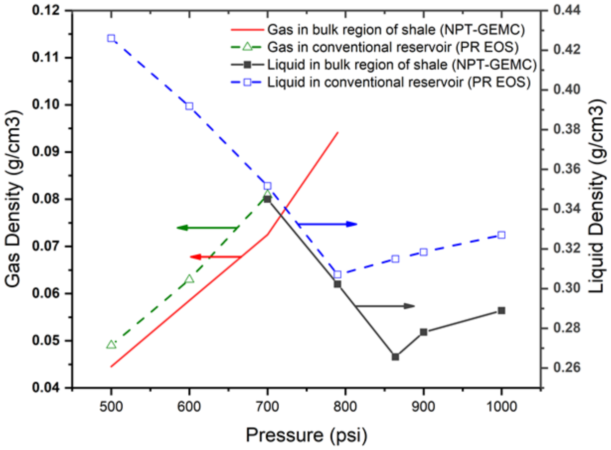

c) Gas and Liquid Densities

Figure 23: Methane/ethane mixture: a). Relative volume in the bulk region of the shale multi-scale model (black) and conventional reservoir condition (blue). b). Liquid saturation in the bulk region of the shale multi-scale model (black) and conventional reservoir condition (blue). c). Gas and liquid densities in the shale multi-scale model (red and black lines, respectively) and conventional reservoir condition (green and blue dashed lines, respectively). Adapted from [80].

To ensure the results from 2,700 molecules are not affected by the total number of molecules, we repeat the same case with the number of molecules doubled. The results of 5,400 molecules are quite similar to the results shown above.

This simulation was also implemented with a lower (20%) and higher (40%) volume fraction of the confined region (Fig. 24). The higher the volume fraction the confined region occupies, the lighter the composition in the bulk region becomes. The bubble point pressure thus increases more. In the 20% and 40% volume fraction cases, the bubble point pressures are 836 and 888 psi, increasing by 5.8% and 12.4%, respectively, compared with the bubble point pressure in a conventional reservoir condition.

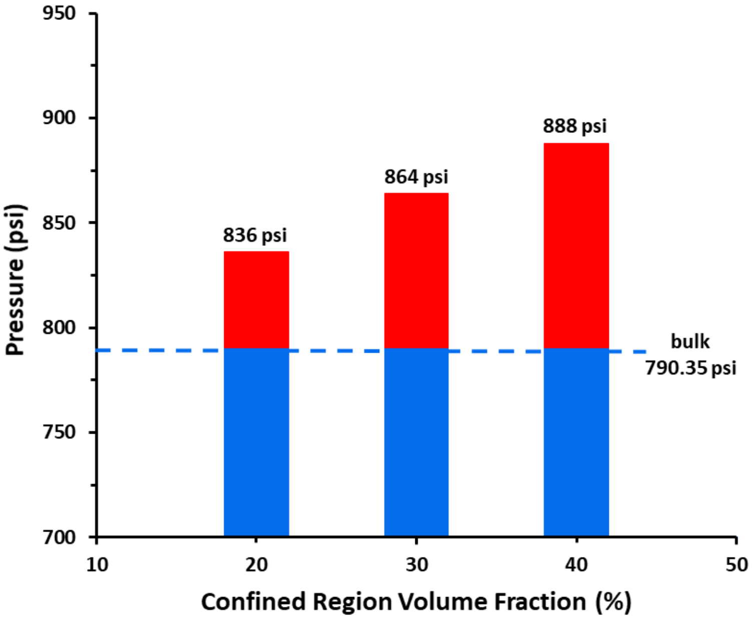

Figure 24: Methane/ethane mixture: The bubble point pressures derived from 20%, 30%, and 40% confined region volume fractions cases by NPT-GEMC simulations. The bubble point pressure in the bulk condition is calculated by PR EOS (blue dashed line and columns). The incremented bubble point pressures in multi-scale models are demonstrated in red columns.

3.3.3. Eagle Ford Gas Condensate Mixture in the Multi-Scale Model

In this case study, we extend the study in the multi-scale model to a more complex reservoir fluid (modified Eagle Ford gas condensate mixture reported in [93]). The assumed reservoir conditions are listed in Table 5. The reservoir temperature is 422.04 K (300°F). The initial reservoir pressure is 4,800 psi. The confined region is built using a nanopore with a diameter of 6 nm and volume contribution of 30%. The reported fluid is first grouped into eight components, which are shown in Table 6. Because we only use real components in the molecular simulation, pseudo-components are then replaced by representative real components. The representative real components are determined by keeping the saturation pressure of the mixture the same. As molecular simulation can only handle an integer number of molecules, the mole fractions of the components used in the simulation have a negligible difference from the reported mole fractions. We use a total of around 5,000 molecules to represent the reported gas condensate mixture. The components, number of the molecule of each species, and mole fractions that are used in the molecular simulation are listed in Table 6. The modified NPT-GEMC method is used to simulate the CCE experiments at the reservoir temperature and a series of pressures ranging from 4,800 psi to 500 psi are simulated to estimate the saturation pressure.

Table 5: Eagle Ford gas condensate reservoir properties. Adapted from [80].

Reservoir Properties	
Fluid type	**Gas condensate**
Initial reservoir pressure (psi)	4800
Reservoir temperature (°F)	300
Confined region volume contribution (%)	30

Table 6: Eagle Ford gas condensate mixture and the number of molecules of each species used in the simulation. Adapted from [80].

Reported		**Simulation**			
Components	**Mole fractions**	**Components**	**Num. of molecules**	**Mole fractions**	**Difference**
C_1	0.70752	**C_1**	3538	0.7077415	0.00022
N_2-C_2	0.09104	**C_2**	455	0.0910182	0.00002
C_3	0.04981	**C_3**	249	0.04981	0.00000
CO_2	0.02885	**CO_2**	144	0.0288058	0.00004
C_4	0.02997	**C_4**	150	0.030006	0.00004
C_5-C_6	0.02209	**C_5**	110	0.0220044	0.00009
C_7-C_{10}	0.04283	**C_8**	214	0.0428086	0.00002
C_{11+}	0.02788	**C_{14}**	139	0.0278056	0.00007
Total	1		4999	1	

To validate the setup of the gas condensate reservoir fluid, we first simulate the CCE experiment in the bulk condition using the NPT-GEMC method. The saturation pressure detected from the simulation is 3,942.5 psi. Compared with the result of 3,940.721 psi calculated by using the PR EOS, the difference is around 0.045%. The same setup is then applied to the multi-scale CCE simulation.

In the multi-scale CCE simulation, the compositions of the fluids in both regions at different pressures are shown in Fig. 25. The simulation starts at 4,800 psi, at which the fluid in the bulk region of the system is in a single phase. The densities of the two simulation boxes that are in the bulk condition are the same. When we reduce the pressure, we observe that the densities of the two bulk boxes are identical throughout the entire process of the CCE experiment simulation. Therefore, there is no two-phase coexistence in the bulk region of the multi-scale system. Taking the composition of the fluid in the bulk area at different pressures to run a flash calculation using PR EOS, the results agree with the molecular simulation. As in the case of the binary mixture study in Section 3.3.2, the composition of the mixture in the bulk region is much leaner than that in the confined region. The lower the pressure goes, the leaner the fluid in the bulk region becomes. The varying composition in the bulk region causes a continuous change of the phase envelope (Fig. 26). Although the pressure further decreases during the process of the CCE experiment simulation, the phase envelope of the mixture in the bulk region keeps shrinking. Consequently, the test points never go into the two-phase region. Therefore, no saturation pressure is detected.

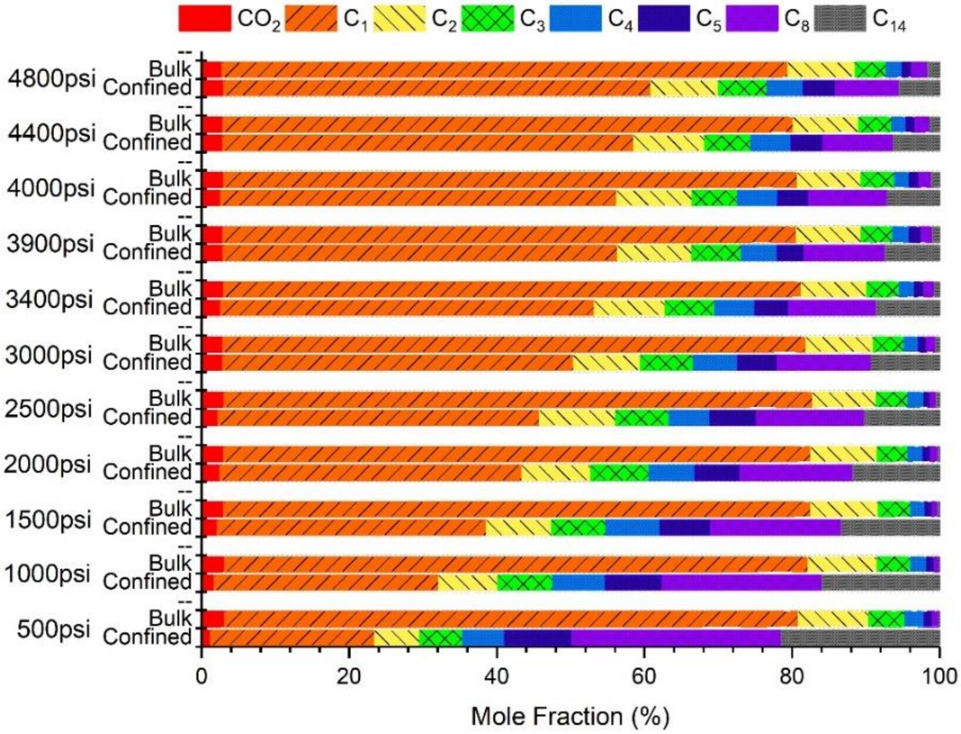

Figure 25: Eagle Ford gas condensate mixture: The compositions of the fluids in the bulk and confined regions at the reservoir temperature. Each color represents a corresponding species. Only the single phase exists in the bulk region during the simulation. No saturation pressure is found in the bulk region. Reprinted from [80].

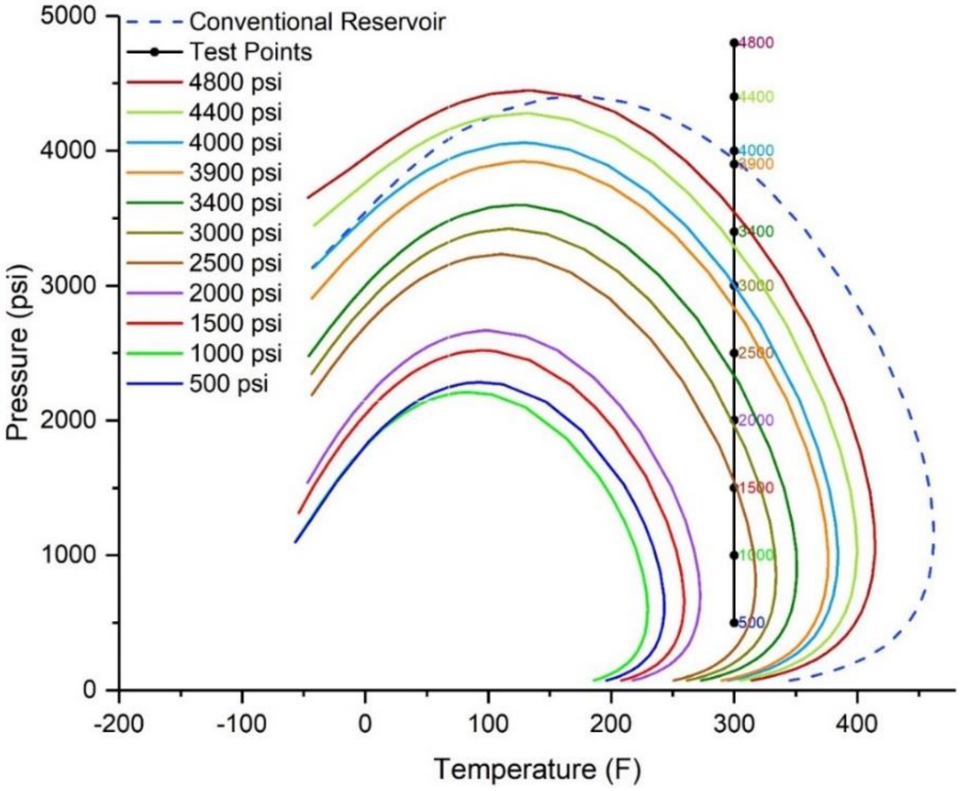

Figure 26: Eagle Ford gas condensate mixture: Pressure–temperature ($P-T$) diagram of the fluid in the bulk region at various pressures. The black line and full circles indicate the reservoir temperature and tested conditions (pressures that simulations are performed at), respectively.

We list the compositions of the fluids in each region as a function of pressure (Fig. 27). For the confined region (Fig. 27a), the mole fractions of the intermediate and heavy components (C_5, C_8, and C_{14}) show a clear trend of increasing as the pressure decreases. That is, as the pressure decreases, the bars for the components C_5, C_8, and C_{14} become longer in the scale. The mole fractions of CO_2, C_1, and C_2, on the other hand, decrease when the pressure decreases. Compared with the mole fraction of C_1 of the feed reservoir fluid in Table 6 which is around 70%, the maximum mole fraction of C_1 in the confined area is only 57.89%. This takes place at the initial reservoir pressure. At 500 psi, the total mole fractions of components C_5, C_8, and C_{14} of the trapped fluid in the confined area can reach more than 50%. The average molecular weight of the confined fluid at 500 psi is around 91.5 g/mol, which increases dramatically compared with the average molecular weight of the original reservoir fluid, which is around 31 g/mol. In terms of the bulk region (Fig. 27b), mole fractions of components C_8 and C_{14} decrease with decreasing pressure, while those of other components except for C_1 fluctuate. The mole fraction of methane increases with decreasing pressure but dips slightly when the pressure is below 1500 psi. It should be noted that at the highest pressure, that is initial pressure at 4,800 psi when the mole fraction of methane is the lowest, the fluid in the bulk region contains 76.68% methane which is around 6% higher than that in the feed composition of the reservoir fluid (see Table 6). Further, the mole fractions of C_5, C_8, and C_{14} are lower than the values in the feed reservoir fluid. Overall, the high mole fractions of methane make the fluid in the bulk region leaner than the original reservoir fluid. As the pressure decreases, the fluid in the bulk region becomes even leaner.

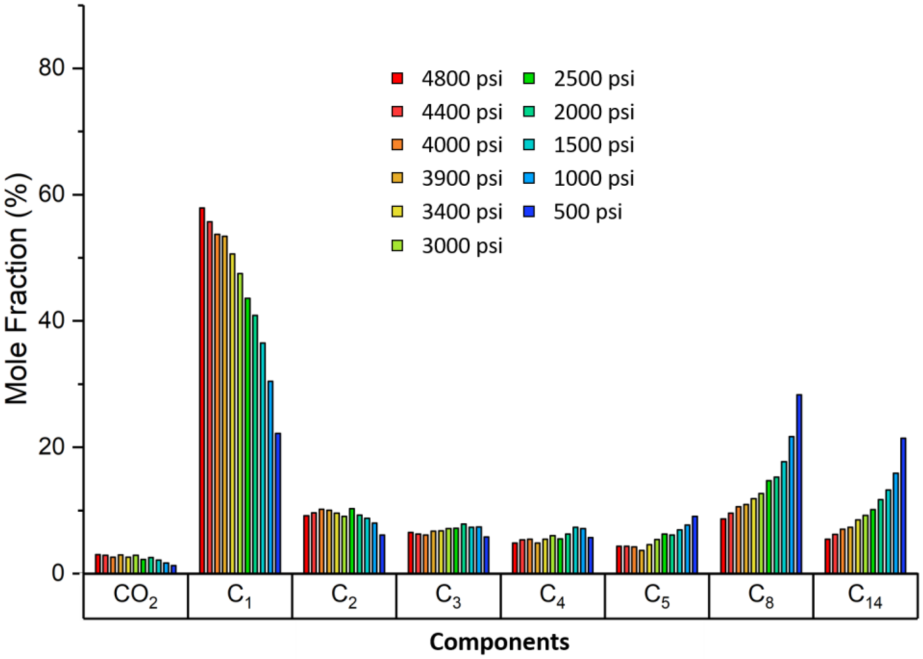

a) Confined Region

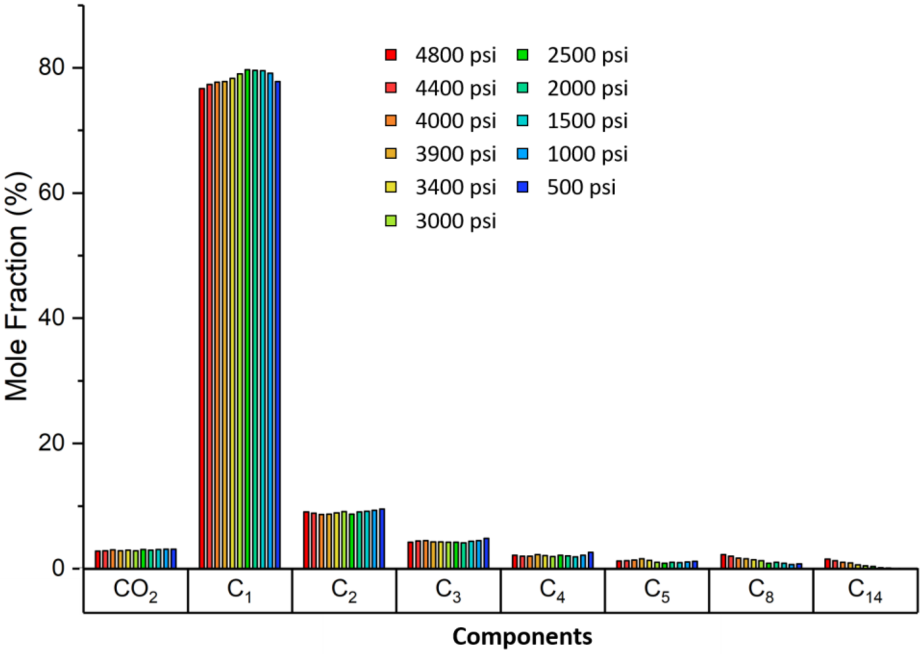

b) Bulk Region

Figure 27: Eagle Ford gas condensate mixture: The mole fractions of different components in the (a) confined and (b) bulk regions at various pressures.

To further investigate the phase behavior of the reservoir fluid, we use the molar density (Fig. 28) to inspect the adsorption (trap) of each species in the confined region. Since the volume of the confined region does not change, changes in the molar density can represent changes in the amount of each species in the confined region. The molar density of the fluid in the bulk region will keep reducing because the volume of the bulk region expands as the pressure decreases. Fig. 28 shows a large amount of reservoir fluid is trapped in the confined region at high pressures. However, light components in the confined region are released to the bulk region as the pressure decreases, while longer chain components are preferably adsorbed at low pressures. Methane, for instance, is released to the bulk region from the nanopore. The amount of methane in the confined region decreases significantly as the pressure drops. Intermediate and heavy components (C_5, C_8, and C_{14}), by contrast, remain trapped in the confined region. The molar densities of C_8 and C_{14} in the confined region increase as the pressure decreases. Similar adsorption behaviors are reported in the work of Jiang et al. [94], Li et al. [95], Lu et al. [96], and Vasileiadis et al. [97]. Assuming the lowest pressure is the ultimate recovery pressure, the trapped components will cause substantially less oil to be produced than a conventional reservoir would, with the same pressure drawdown.

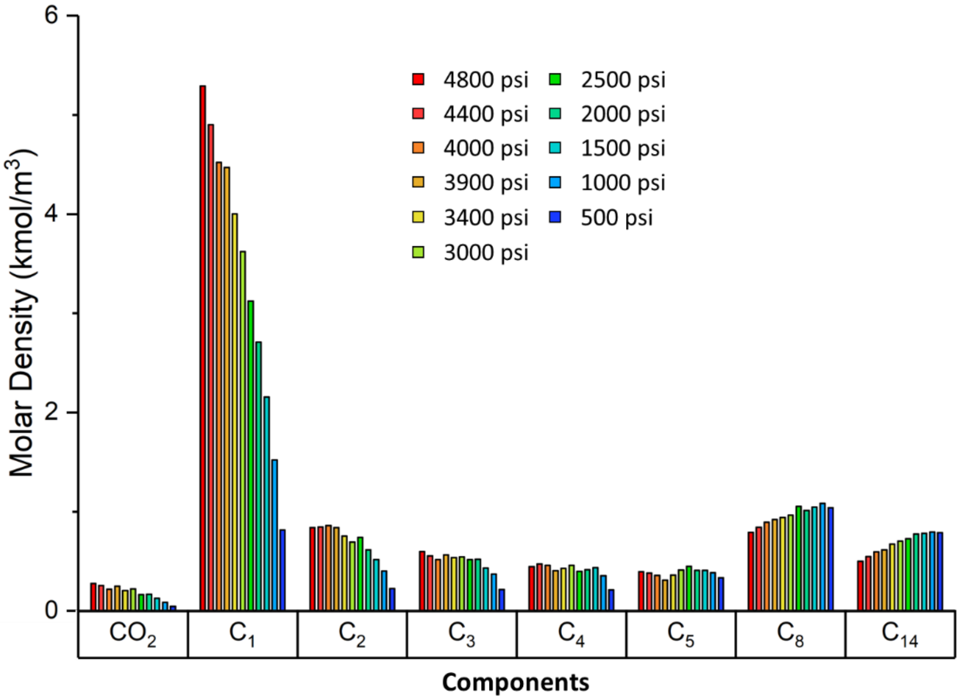

Figure 28: Eagle Ford gas condensate mixture: The molar density profile of the fluid in the confined region at various pressures.

The disappearance of the saturation point is a result of the variation of the composition in the bulk region. The confinement effect in the nanopores causes a difference between the compositions in the bulk and confined regions of the shale multi-scale system. As in the case of the binary mixture study, although the composition in the bulk region continuously varies with the pressure, Fig. 28 indicates that heavier components are more likely to be trapped in the confined region. Accordingly, the fluid in the bulk region is always lighter than that in the confined region. Since the bulk region is more flow effective than the confined region, the fluid that will be produced out of the reservoir will also be lighter and may cause an unexpected high producing GOR compared to the same reservoir fluid in conventional reservoir conditions. Our results are consistent with the observations by Whitson and Sunjerga [4] that the liquid yields in shale reservoirs are always much leaner in comparison with those produced in a conventional reservoir containing the same initial reservoir fluid.

4. SUMMARY AND FUTURE WORK

4.1. Summary

The focus of my study is to investigate the phase behavior of reservoir fluids under the confinement effect. This study uses molecular simulation (Monte Carlo techniques) to explore the fundamentals of the phase behavior of reservoir fluids in nanopores and the reasons why people observe the inconsistency in the phase behavior of fluids in shale reservoirs and conventional reservoirs. Knowledge of this study would improve shale reservoir simulations and production forecasting, and help oil companies make better investment decisions.

The gauge-GEMC simulations are used to investigate the phase behavior of single-component fluids in single cylindrical pore models formed by multi-layer graphite. The phase behavior of methane is studied in nanopores with diameters of 4–10 nm. Results show that in comparison with the bulk condition, at vapor–liquid equilibrium in nanopores, the vapor phase has a dramatically increased density, but the density of the liquid phase is slightly decreased. The confinement effect would cause a shrunk temperature–density diagram with reduced critical temperature and increased critical density. The smaller the pores are, the stronger the confinement effect becomes, and the further the temperature–density diagrams shrink. As the diameter of the pore increases, the phase diagram approaches its bulk values. The pressure–temperature diagrams have demonstrated that the saturation pressure and critical pressure of methane in nanopores are also suppressed from the bulk values.

The pore size distribution (PSD) effect on the phase behavior of methane is further investigated using a multi-pore model, which is generated from discretizing the PSD data from an Eagle Ford sample. According to the configurations of our tests, we demonstrate that the fluids in larger pores would take priority over those in smaller pores in vaporization, while the fluids in smaller pores have priority in condensing. The complex confinement effect in the PSD model can be similar to that of a single-pore model. The temperature–density diagram of the Eagle Ford sample is close to that of a 10 nm cylindrical graphite model.

We have also studied the adsorption isotherm of n-butane in a 2 nm amorphous silica slit pore model using the GCMC simulation. By simulating the adsorption and desorption processes of n-butane in the 2 nm slit pore model, we obtained the condensation pressure (26.66 psi) and vaporization pressure (16.87 psi). The confinement effect causes a strong hysteresis effect. The hysteresis between the phase transition pressures is 9.79 psi. The pressure at which liquid n-butane vaporizes is 36.7% lower than the pressure at which vapor n-butane condenses.

Last but not least, we have created a multi-scale model to capture the complex porous media in shale rocks. The presented model contains the bulk region and the confined region to consider the macro-scale porous media and the nano-scale porous media in shale rocks, respectively. Steele 10-4-3 potential is applied to describe the interactions between fluids molecules and the pore surface in the confined region. Perhaps equally important, we modified the traditional NPT-GEMC technique and used it to simulate the constant composition expansion (CCE) experiments of multicomponent reservoir fluids to measure the saturation pressure. During the CCE experiment simulation, the volume of the confined area is fixed, while the volume of the bulk region changes corresponding to the imposed pressure. The saturation pressure is determined at the point when the phase of the fluid in the bulk region turns from a single phase to two phases. Compositions, saturation pressure, liquid dropout, and the volume of each phase are examined. Because of the confinement effect in the nano-scale porous media, there is a significant difference between the compositions of the fluids in the bulk region and the confined region (the fluid in the bulk region is always leaner than that in the confined region). The compositions of the fluids continuously vary with the pressure. The difference in the compositions increases as the pressure decreases. As a result, the density of the liquid yield is much less than what would be produced from a conventional reservoir containing the same initial reservoir fluid. Assuming that the lowest pressure in the simulation is the ultimate pressure of reservoir development, a substantial amount of intermediate and heavy components remains trapped in the confined region of the shale multi-scale system at the end of the lifetime of the reservoir. The trapped hydrocarbons can lead to a significant recovery loss in the shale reservoir development. In terms of the binary mixture cases, increased bubble point pressures are observed. The amount of the increase is affected by the volume fraction of the confined region. In the Eagle Ford gas condensate mixture case, as the pressure decreases, the fluid in the bulk region of the shale multi-scale system becomes leaner. Consequently, the pressure–temperature phase diagram keeps shrinking. In the presented case, this shrinkage leads to a disappearance of the saturation pressure and a very low condensate yield.

4.2. Future Work

Extensions of the current work can focus on testing and studying the phase behavior of more reservoir fluid types, including black oil and volatile oil field cases. These are also two common producing reservoir fluid types in shale formations. Based on the presented results, we think that there would be a shift in the bubble point pressure and changes in the fluid type along with the production. Besides the CCE experiments, other PVT experiments (e.g., constant volume depletion and differential liberation) can also be simulated by using molecular simulations. Once the change of the saturation pressure and completed confined PVT properties are quantified, as we do for conventional reservoirs, results from the simulations can be used to tune the traditional cubic equation of state (EOS), which has been implemented in the reservoir simulators. By doing this, generated confined PVT tables or properties would improve the accuracy of shale reservoir simulations.

There is no doubt that EOS modeling is the most convenient and efficient technique for computing the phase behavior of reservoir fluids in conventional reservoirs. Copying the success in conventional reservoirs, more and more novel pore-size-dependent EOS's have been developed for shale reservoirs. However, it is difficult to test the accuracy of these correlations using experimental work because of the various limitations in experiments. Molecular simulations, as a middle-solution, can be used to validate and improve the new EOS (if improvements are needed).

More work can be done to improve the efficiency of molecular simulation. Molecular simulations for complex fluid mixtures and systems are time-consuming. This may be the biggest obstacle for the oil and gas industry to implement molecular simulation to field studies. Recent advances in GPUs, parallel computing, and increasing scales of computer architectures make fast work of molecular simulation possible. However, new and advanced algorithms are required for molecular modeling and simulation to make use of the techniques.

REFERENCES

[1] B. Jin, R. Bi, H. Nasrabadi, Molecular simulation of the pore size distribution effect on phase behavior of methane confined in nanopores, Fluid Phase Equilib. (2017). doi:10.1016/j.fluid.2017.08.017.

[2] Y. Pan, R. Bi, P. Zhou, L. Deng, J. Lee, An effective physics-based deep learning model for enhancing production surveillance and analysis in unconventional reservoirs, in: SPE/AAPG/SEG Unconv. Resour. Technol. Conf. 2019, URTC 2019, 2019. doi:10.15530/urtec-2019-145.

[3] S. Luo, J. Lutkenhaus, H. Nasrabadi, A framework for incorporating nanopores in compositional simulation to model the unusually high GOR observed in shale reservoirs, in: Soc. Pet. Eng. - SPE Reserv. Simul. Conf. 2019, RSC 2019, 2019. doi:10.2118/193884-ms.

[4] C.H. Whitson, S. Sunjerga, PVT in Liquid-Rich Shale Reservoirs, SPE Annu. Tech. Conf. Exhib. (2012). doi:10.2118/155499-MS.

[5] M. Khoshghadam, A. Khanal, C. Yu, N. Rabinejadganji, W.J. Lee, Producing gas-oil ratio behavior of unconventional volatile-oil reservoirs, and its application in production diagnostics and decline curve analysis, in: SPE/AAPG/SEG Unconv. Resour. Technol. Conf. 2017, 2017. doi:10.15530/urtec-2017-2670925.

[6] B. Nojabaei, R.T. Johns, L. Chu, Effect of Capillary Pressure on Phase Behavior in Tight Rocks and Shales, SPE Reserv. Eval. Eng. (2013). doi:10.2118/159258-PA.

[7] R. Cao, L. Ma, A. Blount, Maximizing the value of unconventional liquid rich shale development with integrated cross-discipline approach, in: Soc. Pet. Eng. - SPE Liq. - Rich Basins Conf. - North Am. 2016, 2016. doi:10.2118/181768-ms.

[8] R.S. Jones, Producing-Gas/Oil-Ratio Behavior of Multifractured Horizontal Wells in Tight Oil Reservoirs, SPE Reserv. Eval. Eng. (2017). doi:10.2118/184397-pa.

[9] C.R. Clarkson, N. Solano, R.M. Bustin, A.M.M. Bustin, G.R.L. Chalmers, L. He, Y.B. Melnichenko, A.P. Radliński, T.P. Blach, Pore structure characterization of North American shale gas reservoirs using USANS/SANS, gas adsorption, and mercury intrusion, Fuel. (2013). doi:10.1016/j.fuel.2012.06.119.

[10] J. Rouquerolt, D. Avnir, C.W. Fairbridge, D.H. Everett, J.H. Haynes, N. Pernicone, J.D.F. Ramsay, K.S.W. Sing, K.K. Unger, Recommendations for the characterization of porous solids, Pure Appl. Chem. 66 (1994) 1739–1758. doi:10.1351/pac199466081739.

[11] R.F. Sigal, Pore-Size Distributions for Organic-Shale-Reservoir Rocks From Nuclear-Magnetic-Resonance Spectra Combined With Adsorption Measurements, SPE J. (2015). doi:10.2118/174546-PA.

[12] D.Y. Peng, D.B. Robinson, A New Two-Constant Equation of State, Ind. Eng. Chem. Fundam. (1976). doi:10.1021/i160057a011.

[13] R. Bi, A. Zidane, A. Firoozabadi, Efficient and robust stability analysis in the internal energy, volume, and moles (UVN) space, Fluid Phase Equilib. (2020). doi:10.1016/j.fluid.2020.112468.

[14] G. Soave, Equilibrium constants from a modified Redlich-Kwong equation of

state, Chem. Eng. Sci. (1972). doi:10.1016/0009-2509(72)80096-4.

[15] B. Jin, H. Nasrabadi, Phase behavior in shale organic/inorganic nanopores from molecular simulation, SPE Reserv. Eval. Eng. (2018). doi:10.2118/187307-PA.

[16] S. Luo, J.L. Lutkenhaus, H. Nasrabadi, Multiscale Fluid-Phase-Behavior Simulation in Shale Reservoirs Using a Pore-Size-Dependent Equation of State, SPE Reserv. Eval. Eng. 21 (2018) 0806–0820. doi:10.2118/187422-pa.

[17] Q. Yang, B. Jin, D. Banerjee, H. Nasrabadi, Direct visualization and molecular simulation of dewpoint pressure of a confined fluid in sub-10 nm slit pores, Fuel. 235 (2019) 1216–1223. doi:10.1016/j.fuel.2018.08.050.

[18] Z. Jin, A. Firoozabadi, Thermodynamic Modeling of Phase Behavior in Shale Media, Soc. Pet. Eng. J. (2016). doi:10.2118/176015-PA.

[19] Y. Zhang, D. Shao, J. Yan, X. Jia, Y. Li, P. Yu, T. Zhang, The pore size distribution and its relationship with shale gas capacity in organic-rich mudstone of Wufeng-Longmaxi Formations, Sichuan Basin, China, J. Nat. Gas Geosci. (2016). doi:10.1016/j.jnggs.2016.08.002.

[20] A. Al Hinai, R. Rezaee, L. Esteban, M. Labani, Comparisons of pore size distribution: A case from the Western Australian gas shale formations, J. Unconv. Oil Gas Resour. (2014). doi:10.1016/j.juogr.2014.06.002.

[21] U. Kuila, M. Prasad, Specific surface area and pore-size distribution in clays and shales, Geophys. Prospect. 61 (2013) 341–362. doi:10.1111/1365-2478.12028.

[22] M. Thommes, G.H. Findenegg, Pore Condensation and Critical-Point Shift of a Fluid in Controlled-Pore Glass, Langmuir. (1994). doi:10.1021/la00023a058.

[23] A. de Keizer, T. Michalski, G.H. Findenegg, Fluids in pores: experimental and computer simulation studies of multilayer adsorption, pore condensation and critical-point shifts, Pure Appl. Chem. (2007). doi:10.1351/pac199163101495.

[24] P.J. Branton, P.G. Hall, M. Treguer, K.S.W. Sing, Adsorption of carbon dioxide, sulfur dioxide and water vapour by MCM-41, a model mesoporous adsorbent, J. Chem. Soc. Faraday Trans. (1995). doi:10.1039/FT9959102041.

[25] S.Z. Qiao, S.K. Bhatia, D. Nicholson, Study of Hexane Adsorption in Nanoporous MCM-41 Silica, Langmuir. (2004). doi:10.1021/la0353430.

[26] M. Pathak, H. Cho, M. Deo, Experimental and Molecular Modeling Study of Bubble Points of Hydrocarbon Mixtures in Nanoporous Media, Energy and Fuels. (2017). doi:10.1021/acs.energyfuels.6b02422.

[27] K. Morishige, M. Ito, Capillary condensation of nitrogen in MCM-41 and SBA-15, J. Chem. Phys. (2002). doi:10.1063/1.1510440.

[28] J.H. Yun, T. Düren, F.J. Keil, N.A. Seaton, Adsorption of methane, ethane, and their binary mixtures on MCM-41: Experimental evaluation of methods for the prediction of adsorption equilibrium, Langmuir. (2002). doi:10.1021/la0155855.

[29] S. Luo, J.L. Lutkenhaus, H. Nasrabadi, Experimental Study of Confinement Effect on Hydrocarbon Phase Behavior in Nano-Scale Porous Media Using Differential Scanning Calorimetry, in: SPE Annu. Tech. Conf. Exhib., 2015. doi:10.2118/175095-MS.

[30] S. Luo, J.L. Lutkenhaus, H. Nasrabadi, Use of differential scanning calorimetry to study phase behavior of hydrocarbon mixtures in nano-scale porous media, J. Pet.

Sci. Eng. (2016). doi:10.1016/j.petrol.2016.12.019.

[31] S. Luo, J.L. Lutkenhaus, H. Nasrabadi, Confinement-Induced Supercriticality and Phase Equilibria of Hydrocarbons in Nanopores, Langmuir. (2016). doi:10.1021/acs.langmuir.6b03177.

[32] S. Luo, H. Nasrabadi, J.L. Lutkenhaus, Effect of confinement on the bubble points of hydrocarbons in nanoporous media, AIChE J. (2016). doi:10.1002/aic.15154.

[33] M. Alfi, H. Nasrabadi, D. Banerjee, Experimental investigation of confinement effect on phase behavior of hexane, heptane and octane using lab-on-a-chip technology, Fluid Phase Equilib. (2016). doi:10.1016/j.fluid.2016.04.017.

[34] B. Bao, J. Riordon, Y. Xu, H. Li, D. Sinton, Direct Measurement of the Fluid Phase Diagram, Anal. Chem. (2016). doi:10.1021/acs.analchem.6b01725.

[35] F. Mostowfi, S. Molla, P. Tabeling, Determining phase diagrams of gas-liquid systems using a microfluidic PVT, Lab Chip. (2012). doi:10.1039/c2lc40706j.

[36] B. Pinho, S. Girardon, F. Bazer-Bachi, G. Bergeot, S. Marre, C. Aymonier, A microfluidic approach for investigating multicomponent system thermodynamics at high pressures and temperatures, Lab Chip. (2014). doi:10.1039/c4lc00505h.

[37] S. Molla, F. Mostowfi, Microfluidic platform for PVT measurements, in: Proc. - SPE Annu. Tech. Conf. Exhib., 2014. doi:10.2118/170910-ms.

[38] L. Wang, E. Parsa, Y. Gao, J.T. Ok, K. Neeves, X. Yin, E. Ozkan, Experimental study and modeling of the effect of nanoconfinement on hydrocarbon phase behavior in unconventional reservoirs, in: Soc. Pet. Eng. West. North Am. Rocky Mt. Jt. Conf. Exhib. 2014, 2014. doi:10.2118/169581-ms.

[39] E. Parsa, X. Yin, E. Ozkan, Direct observation of the impact of nanopore confinement on petroleum gas condensation, in: Proc. - SPE Annu. Tech. Conf. Exhib., 2015. doi:10.2118/175118-ms.

[40] J. Zhong, S.H. Zandavi, H. Li, B. Bao, A.H. Persad, F. Mostowfi, D. Sinton, Condensation in One-Dimensional Dead-End Nanochannels, ACS Nano. (2017). doi:10.1021/acsnano.6b05666.

[41] C. Duan, A. Majumdar, Anomalous ion transport in 2-nm hydrophilic nanochannels, Nat. Nanotechnol. (2010). doi:10.1038/nnano.2010.233.

[42] N. Siripatrachai, T. Ertekin, R. Johns, Compositional Simulation of Discrete Fractures Incorporating the Effect of Capillary Pressure on Phase Behavior, in: SPE Improv. Oil Recover. Conf., 2016. doi:10.2118/179660-MS.

[43] L. Du, L. Chu, Understanding Anomalous Phase Behavior in Unvonventional Oil Reservoirs, SPE Can. Unconv. Resour. Conf. (2012). doi:10.2118/161830-MS.

[44] L. Jin, Y. Ma, A. Jamili, Investigating The Effect of Pore Proximity on Phase Behavior And Fluid Properties in Shale Formations, in: SPE Annu. Tech. Conf. Exhib., 2013. doi:10.2118/166192-MS.

[45] Y. Zhang, W. Yu, K. Sepehrnoori, Y. Di, Investigation of nanopore confinement on fluid flow in tight reservoirs, J. Pet. Sci. Eng. (2017). doi:10.1016/j.petrol.2016.11.005.

[46] B. Nojabaei, N. Siripatrachai, R.T. Johns, T. Ertekin, Effect of large gas-oil capillary pressure on production: A compositionally-extended black oil formulation, J. Pet. Sci. Eng. (2016). doi:10.1016/j.petrol.2016.05.048.

[47] D. Devegowda, K. Sapmanee, F. Civan, R.F. Sigal, Phase Behavior of Gas Condensates in Shales Due to Pore Proximity Effects: Implications for Transport, Reserves and Well Productivity, in: SPE Annu. Tech. Conf. Exhib., 2012. doi:10.2118/160099-MS.

[48] N.S. Alharthy, T. Nguyen, T. Teklu, H. Kazemi, R. Graves, Multiphase Compositional Modeling in Small-Scale Pores of Unconventional Shale Reservoirs, in: SPE Annu. Tech. Conf. Exhib., 2013. doi:10.2118/166306-MS.

[49] L. Travalloni, M. Castier, F.W. Tavares, Phase equilibrium of fluids confined in porous media from an extended Peng-Robinson equation of state, Fluid Phase Equilib. (2014). doi:10.1016/j.fluid.2013.10.049.

[50] Z. Li, Z. Jin, A. Firoozabadi, Phase Behavior and Adsorption of Pure Substances and Mixtures and Characterization in Nanopore Structures by Density Functional Theory, SPE J. (2014). doi:10.2118/169819-PA.

[51] S.K. Singh, A. Sinha, G. Deo, J.K. Singh, Vapor− liquid phase coexistence, critical properties, and surface tension of confined alkanes, J. Phys. Chem. C. (2009). doi:10.1021/jp8073915.

[52] Z. Jin, A. Firoozabadi, Phase behavior and flow in shale nanopores from molecular simulations, Fluid Phase Equilib. (2016). doi:10.1016/j.fluid.2016.09.011.

[53] P. Ungerer, B. Tavitian, A. Boutin, Applications of molecular simulation in the oil and gas industry: Monte Carlo methods, Editions Technip, 2005.

[54] N. Metropolis, A.W. Rosenbluth, M.N. Rosenbluth, A.H. Teller, E. Teller,

Equation of state calculations by fast computing machines, J. Chem. Phys. (1953). doi:10.1063/1.1699114.

[55] I.R. McDonald, NpT-ensemble monte carlo calculations for binary liquid mixtures, Mol. Phys. (1972). doi:10.1080/00268977200100031.

[56] A.Z. Panagiotopoulos, U.W. Suter, R.C. Reid, Phase diagrams of nonideal fluid mixtures from Monte Carlo simulation, Ind. Eng. Chem. Fundam. 25 (1986) 525–535. doi:10.1021/i100024a012.

[57] M.H. Lagache, P. Ungerer, A. Boutin, Prediction of thermodynamic derivative properties of natural condensate gases at high pressure by Monte Carlo simulation, Fluid Phase Equilib. (2004). doi:10.1016/j.fluid.2004.03.015.

[58] B. Neubauer, A. Boutin, B. Tavitian, A.H. Fuchs, Gibbs ensemble simulations of vapour—liquid phase equilibria of cyclic alkanes, Mol. Phys. 97 (1999) 769–776. doi:10.1080/00268979909482877.

[59] L.A. Rowley, D. Nicholson, N.G. Parsonage, Monte Carlo grand canonical ensemble calculation in a gas-liquid transition region for 12-6 Argon, J. Comput. Phys. (1975). doi:10.1016/0021-9991(75)90042-X.

[60] B. Coasne, K.E. Gubbins, R.J.M. Pellenq, Temperature effect on adsorption/desorption isotherms for a simple fluid confined within various nanopores, in: Adsorption, 2005. doi:10.1007/s10450-005-5939-y.

[61] B. Libby, P.A. Monson, Adsorption/desorption hysteresis in inkbottle pores: A density functional theory and Monte Carlo simulation study, Langmuir. (2004). doi:10.1021/la036100a.

[62] B. Jin, H. Nasrabadi, Phase behavior of multi-component hydrocarbon systems in nano-pores using gauge-GCMC molecular simulation, Fluid Phase Equilib. (2016). doi:10.1016/j.fluid.2016.06.018.

[63] A.Z. Panagiotopoulos, Direct determination of phase coexistence properties of fluids by Monte Carlo simulation in a new ensemble, Mol. Phys. (1987). doi:10.1080/00268977011009786.

[64] B. Smit, P. De Smedt, D. Frenkel, Computer simulations in the gibbs ensemble, Mol. Phys. (1989). doi:10.1080/00268978900102641.

[65] A. Neimark, a Vishnyakov, Gauge cell method for simulation studies of phase transitions in confined systems, Phys. Rev. E. Stat. Phys. Plasmas. Fluids. Relat. Interdiscip. Topics. (2000). doi:10.1103/PhysRevE.62.4611.

[66] A. Vishnyakov, A. V. Neimark, Studies of liquid-vapor equilibria, criticality, and spinodal transitions in nanopores by the gauge cell Monte Carlo simulation method, J. Phys. Chem. B. (2001). doi:10.1021/jp003994o.

[67] A. Vishnyakov, A. V. Neimark, Multicomponent gauge cell method, J. Chem. Phys. (2009). doi:10.1063/1.3124186.

[68] A.Z. Panagiotopoulos, N. Quirke, M. Stapleton, D.J. Tildesley, Phase equilibria by simulation in the gibbs ensemble alternative derivation, generalization and application to mixture and membrane equilibria, Mol. Phys. (1988). doi:10.1080/00268978800100361.

[69] J.J. Potoff, J.I. Siepmann, Vapor–liquid equilibria of mixtures containing alkanes, carbon dioxide, and nitrogen, AIChE J. (2001). doi:10.1002/aic.690470719.

[70] I. Nikolaidis, A. Poursaeidesfahani, … Z.C.-Aic., U. 2019, Modeling the phase equilibria of asymmetric hydrocarbon mixtures using molecular simulation and equations of state, Wiley Online Libr. (2018). doi:10.1002/aic.16453.

[71] W.A. Steele, The Physical Interaction of Gases with Crystalline Solids, North-Holl. Publ. Co. (1973). doi:10.1016/0039-6028(73)90264-1.

[72] W.A. Steele, The interaction of rare gas atoms with graphitized carbon black, J. Phys. Chem. (1978). doi:10.1021/j100496a011.

[73] M.W. Maddox, S.L. Sowers, K.E. Gubbins, Molecular simulation of binary mixture adsorption in buckytubes and MCM-41, Adsorption. (1996). doi:10.1007/BF00127095.

[74] L.D. Gelb, K.E. Gubbins, R. Radhakrishnan, M. Sliwinska-Bartkowiak, Phase separation in confined systems, Reports Prog. Phys. (1999). doi:10.1088/0034-4885/62/12/201.

[75] D.W. Siderius, L.D. Gelb, Extension of the Steele 10-4-3 potential for adsorption calculations in cylindrical, spherical, and other pore geometries, J. Chem. Phys. (2011). doi:10.1063/1.3626804.

[76] M.G. Martin, A.L. Frischknecht, Using arbitrary trial distributions to improve intramolecular sampling in configurational-bias Monte Carlo, Mol. Phys. (2006). doi:10.1080/00268970600751078.

[77] B. Widom, Some Topics in the Theory of Fluids, J. Chem. Phys. (1963). doi:10.1063/1.1734110.

[78] B. Widom, Potential-distribution theory and the statistical mechanics of fluids, J.

Phys. Chem. (1982). doi:10.1021/j100395a005.

[79] K.S. Shing, S.T. Chung, Computer Simulation Methods for the Calculation of Solubility in Supercritical Extraction Systems, J. Phys. Chem. J. Am. Chem. Soc. Chem. Sac. J. Phys. Chem. (1987). doi:10.1021/j100290a077.

[80] R. Bi, H. Nasrabadi, Molecular simulation of the constant composition expansion experiment in shale multi-scale systems, Fluid Phase Equilib. 495 (2019) 59–68. doi:10.1016/J.FLUID.2019.04.026.

[81] A. Firoozabadi, Thermodynamics of hydrocarbon reservoirs, McGraw-Hill, 1999.

[82] S. Reif-Acherman, The history of the rectilinear diameter law, Quim. Nova. (2010). doi:10.1590/S0100-40422010000900033.

[83] J.A. Zoll Weg, G.W. Mulholland, On the law of the rectilinear diameter, J. Chem. Phys. (1972). doi:10.1063/1.1678352.

[84] R. Scott, M.P. Allen, D.J. Tildesley, Computer Simulation of Liquids., Math. Comput. (1991). doi:10.2307/2938686.

[85] K.E. Gubbins, Y. Long, M. Śliwinska-Bartkowiak, Thermodynamics of confined nano-phases, J. Chem. Thermodyn. (2014). doi:10.1016/j.jct.2014.01.024.

[86] M.G. Martin, J.I. Siepmann, Transferable potentials for phase equilibria. 1. United-atom description of n-alkanes, J. Phys. Chem. B. (1998). doi:10.1021/jp972543+.

[87] P. Van Der Ploeg, H.J.C. Berendsen, Molecular dynamics simulation of a bilayer membrane, J. Chem. Phys. (1982). doi:10.1063/1.443321.

[88] M.G. Martin, MCCCS Towhee: A tool for monte carlo molecular simulation,

Mol. Simul. (2013). doi:10.1080/08927022.2013.828208.

[89] R.G. Loucks, R.M. Reed, S.C. Ruppel, D.M. Jarvie, Morphology, Genesis, and Distribution of Nanometer-Scale Pores in Siliceous Mudstones of the Mississippian Barnett Shale, J. Sediment. Res. (2009). doi:10.2110/jsr.2009.092.

[90] R.G. Loucks, R.M. Reed, S.C. Ruppel, U. Hammes, Spectrum of pore types and networks in mudrocks and a descriptive classification for matrix-related mudrock pores, Am. Assoc. Pet. Geol. Bull. (2012). doi:10.1306/08171111061.

[91] M.E. Curtis, R.J. Ambrose, C.H. Sondergeld, C.S. Rai, Structural characterization of gas shales on the micro- and nano-scales, in: Soc. Pet. Eng. - Can. Unconv. Resour. Int. Pet. Conf. 2010, 2010. doi:10.2118/137693-ms.

[92] W.D. Mccain, Jr, The Properties of Petroleum Fluids, 2 nd Ed, PennWell Books, Tulsa. (1990). doi:TN870.5.M386.

[93] A. Orangi, N.R. Nagarajan, M.M. Honarpour, J.J. Rosenzweig, Unconventional Shale Oil and Gas-Condensate Reservoir Production, Impact of Rock, Fluid, and Hydraulic Fractures, in: SPE Hydraul. Fract. Technol. Conf., 2011. doi:10.2118/140536-MS.

[94] J. Jiang, S.I. Sandler, M. Schenk, B. Smit, Adsorption and separation of linear and branched alkanes on carbon nanotube bundles from configurational-bias Monte Carlo simulation, Phys. Rev. B. (2005). doi:10.1103/PhysRevB.72.045447.

[95] W.Z. Li, Z.Y. Liu, Y.L. Che, D. Zhang, Molecular simulation of adsorption and separation of mixtures of short linear alkanes in pillared layered materials at ambient temperature, J. Colloid Interface Sci. (2007).

doi:10.1016/j.jcis.2007.04.014.

[96] L. Lu, Q. Wang, Y. Liu, Adsorption and separation of ternary and quaternary mixtures of short linear alkanes in zeolites by molecular simulation, Langmuir. (2003). doi:10.1021/la034766z.

[97] M. Vasileiadis, L.D. Peristeras, K.D. Papavasileiou, I.G. Economou, Transport Properties of Shale Gas in Relation to Kerogen Porosity, J. Phys. Chem. C. 122 (2018) 6166–6177. doi:10.1021/acs.jpcc.8b00162.

APPENDIX A

AN EXAMPLE OF THE INPUT FILE FOR N-BUTANE ADSORPTION

An example of the input file for the adsorption isotherm study of n-butane using the 2 nm amorphous silica slit pore model is presented in this section. The model contains 634 oxygen atoms and 274 silicon atoms as the amorphous silica slit pore boundaries. The simulation was performed using the GCMC ensemble with the chemical potential $\mu_{\mathrm{nC_4}}/k_B = -2400$ K. The input file is as follows:

```
inputformat
'Towhee'
ensemble
'uvt'
temperature
298.15
nmolty
3
nmolectyp
634 274 10000
chempot
0 0 -2400
numboxes
1
lperiod_xyz
.true. .true. .false.
wall_thick
10.0
stepstyle
'moves'
nstep
4000000
printfreq
10000
blocksize
500000
moviefreq
0
backupfreq
100000
runoutput
'blocks'
pdb_output_freq
500000
```

```
pressurefreq
100000
trmaxdispfreq
00
volmaxdispfreq
00
chempotperstep
0  0  1
potentialstyle
'internal'
ffnumber
2
ff_filename
/home/ranb/towhee-7.0.6/ForceFields/towhee_ff_TraPPE-UA
/scratch/user/ranb/Quartz_alpha/nC4_Slit8_040_25.2C/towhee_ff_Charmm
classical_potential
'Lennard-Jones'
classical_mixrule
'Lorentz-Berthelot'
lshift
.false.
ltailc
.true.
rmin
1.0d0
rcut
9.0d0
rcutin
5.0d0
electrostatic_form
'coulomb'
coulombstyle
'ewald_fixed_kmax'
kalp
5.6
kmax
5
dielect
1.0
linit
.true.
initboxtype
'dimensions'
initstyle
```

```
'coords' 'coords' 'coords'
initlattice
'none' 'none' 'none'
initmol
634 274 0000
inix iniy iniz
100   100   100
hmatrix
40d0 0.0d0 0.0d0
0.0d0 40.00d0 0.0d0
0.0d0 0.0d0  40.0d0
n_hole
0
hole_dimen
pmuvtcbswap
0.6
          pmuvtcbmt
          0.0  0.0  1.0
pmcb
0.8
          pmcbmt
          0.0  0.0  1.0
          pmall
          0.0  0.0  0.5
pmcomposite
1.00d0
       pmcomt
       0.0 0.0 1.0
       rmcomtra
       10d0
       rmcomrot
       5d0
cbmc_formulation
'Martin and Frischknecht 2006'
cbmc_setting_style
'Martin and Frischknecht'
wall_type
1
input_style
'basic connectivity map'
nunit
1
nmaxcbmc
1
```

```
lpdbnames
T
forcefield
'ClayFF'
charge_assignment
'bond increment'
unit ntype
1    'ob'
pdbname aminonum aminoshort
O 1 OXY
vibration
0
improper
0
wall_type
1
input_style
'basic connectivity map'
nunit
1
nmaxcbmc
1
lpdbnames
T
forcefield
'ClayFF'
charge_assignment
'bond increment'
unit ntype
1    'st'
pdbname aminonum aminoshort
SI 2 SIL
vibration
0
improper
0
wall_type
0
input_style
'basic connectivity map'
nunit
4
nmaxcbmc
4
```

```
lpdbnames
T
forcefield
'TraPPE-UA'
charge_assignment
'bond increment'
unit ntype
1    'CH3*(sp3)'
pdbname aminonum aminoshort
NC4 3 BUT
vibration
1
2
improper torsion
0
unit ntype
2    'CH2**(sp3)'
pdbname aminonum aminoshort
NC4 3 BUT
vibration
2
1 3
improper torsion
0
unit ntype
3    'CH2**(sp3)'
pdbname aminonum aminoshort
NC4 3 BUT
vibration
2
2 4
improper torsion
0
unit ntype
4    'CH3*(sp3)'
pdbname aminonum aminoshort
NC4 3 BUT
vibration
1
3
improper torsion
0
```

APPENDIX B

AN EXAMPLE OF THE INPUT FILE FOR METHANE USING THE EAGLE FORD PORE SIZE DISTRIBUTION MODEL

An example of the input file for the vapor-liquid equilibrium study of methane using the Eagle Ford pore size distribution model is presented in this section. The pore size distribution model contains 18,135 carbon atoms as the multi-layer graphite cylindrical pore boundaries. The simulation was performed using the gauge-GEMC ensemble with 3,750 methane molecules at 140 K. The input file is as follows:

```
inputformat
'Towhee'
ensemble
'nvt'
temperature
140
nmolty
2
nmolectyp
18135 03750
numboxes
2
lperiod_xyz
.false. .false. .true.
.true. .true. .true.
wall_thick
0.0
0.0
stepstyle
'moves'
nstep
4000000
printfreq
1000
blocksize
500000
moviefreq
0
backupfreq
100000
runoutput
blocks
```

```
pdb_output_freq
2000000
pressurefreq
00000
trmaxdispfreq
000
volmaxdispfreq
000
chempotperstep
0  1
potentialstyle
'internal'
ffnumber
1
ff_filename
/home/ranb/towhee-7.0.6/ForceFields/towhee_ff_TraPPE-UA
classical_potential
'Lennard-Jones'
classical_mixrule
'Lorentz-Berthelot'
lshift
.false.
ltailc
.true.
rmin
1.0d0
rcut
20.0d0
rcutin
5.0d0
electrostatic_form
'none'
linit
.true.
initboxtype
'dimensions'
initstyle
'coords' 'coords'
'full cbmc' 'full cbmc'
initlattice
'none' 'none'
'simple cubic' 'simple cubic'
initmol
18135 0
```

```
0000 03750
inix iniy iniz
100  100  100
30   30   30
hmatrix
300d0 0.0d0 0.0d0
0.0d0   140d0  0.0d0
0.0d0 0.0d0  40.2d0
55d0 0.0d0 0.0d0
0.0d0   55d0  0.0d0
0.0d0 0.0d0  55d0
n_hole
5  0
hole_dimen
35   35 0.0 40.2  30
35   100 0.0 40.2  25
115   25 0.0 40.2  20
115   95 0.0 40.2  40
230   70 0.0 40.2  65
pm2boxcbswap
0.50d0
        pm2cbswmt
        0.0 1.0d0
           pm2cbswpr
           1.0
pmtracm
1.00d0
        pmtcmt
        0.0 1.0d0
        rmtrac
        40d0
        tatrac
        0.5d0
cbmc_formulation
'Martin and Frischknecht 2006'
cbmc_setting_style
'Martin and Frischknecht'
wall_type
1
input_style
'basic connectivity map'
nunit
1
nmaxcbmc
```

```
1
lpdbnames
F
forcefield
'TraPPE-UA'
charge_assignment
'bond increment'
unit ntype
1    'Caaa(aro)'
vibration
0
improper
0
wall_type
0
input_style
'basic connectivity map'
nunit
1
nmaxcbmc
1
lpdbnames
F
forcefield
'TraPPE-UA'
charge_assignment
'bond increment'
unit ntype
1    'CH4'
vibration
0
improper torsion
0
```